The GSI Capability to Assimilate TRMM and GPM Hydrometeor Retrievals in HWRF

Ting-Chi Wu[*a], Milija Zupanski[a], Lewis D. Grasso[a], Paula P. Brown[b], Christian D. Kummerow[a,b], and John A. Knaff[c]

[a]Cooperative Institute for Research in the Atmosphere (CIRA), Colorado State University
Fort Collins, Colorado

[b]Department of Atmospheric Science, Colorado State University
Fort Collins, Colorado

[c]NOAA/Center for Satellite Applications and Research
Fort Collins, Colorado

Revised for Publication in Quarterly Journal of The Royal Meteorological Society on June 2nd, 2016

Keywords: Satellite Data Assimilation; TRMM; GPM; Hurricane Forecasting; HWRF

Running Head: Assimilating TRMM/GPM retrieved hydrometeors in HWRF

[*]Correspondence to T.-C. Wu, Cooperative Institute for Research in the Atmosphere, Colorado State University, 1375 Campus Delivery, Fort Collins, CO 80521, USA.
E-mail: Ting-Chi.Wu@colostate.edu

ABSTRACT

Hurricane forecasting skills may be improved by utilizing increased precipitation observations available from the Global Precipitation Mission (GPM). This study adds to the GSI capability to assimilate satellite retrieved hydrometeor profile data in the operational HWRF system. The newly developed Hurricane GPROF algorithm produces TRMM/GPM hydrometeor retrievals specifically for hurricanes. Two new observation operators are developed and implemented in GSI to assimilate Hurricane GPROF retrieved hydrometeors in HWRF. They are based on the assumption that all water vapor in excess of saturation with respect to ice or liquid is immediately condensed out. Two sets of single observation experiments that include assimilation of solid or liquid hydrometeor from Hurricane GPROF are performed. Results suggest that assimilating single retrieved solid or liquid hydrometeor information impacts the current set of control variables of GSI by adjusting the environment that includes temperature, pressure, and moisture fields toward saturation with respect to ice or liquid. These results are explained in a physically consistent manner, implying satisfactory observation operators and meaningful structure of background error covariance employed by GSI. Applying to two real hurricane cases, Leslie (2012) and Gonzalo (2014), the assimilation of the Hurricane GPROF data in the innermost domain of HWRF shows a physically reasonable adjustment and an improvement of the analysis compared to observations. However, the impact of assimilating the Hurricane GPROF retrieved hydrometeors on the subsequent

HWRF forecasts, measured by hurricane tracks, intensities, sizes, satellite retrieved rain rates, and corresponding IR images, is inconclusive. Possible causes are discussed.

1. INTRODUCTION

One of the most urgent goals in the National Oceanographic and Atmospheric Administration (NOAA), National Centers for Environmental Prediction (NCEP), and many other international numerical weather prediction (NWP) centers is to improve hurricane forecasts (e.g., NOAA, 2010). In addition to hurricane track and intensity predictions, precipitation forecasts have received significant attention due to the high-impact flooding and/or landslides from heavy rains worldwide (e.g., Yu et al. 2014). With more satellite precipitation observations available through the GPM constellation, NWP hurricane forecasting skills may be improved via data assimilation. A combination of existing regional hurricane models and advanced data assimilation techniques are well suited to take advantage of the additional satellite precipitation observations. One available tool is the Hurricane Weather Research and Forecasting model (HWRF) that utilizes not only an advanced data assimilation component, but also a forecasting component (Tallapragada et al., 2014).

HWRF is a coupled atmosphere-ocean dynamic forecast model that is run operationally by NCEP to support the National Hurricane Center (NHC) on the tropical cyclone track

and intensity forecast guidance (Rappaport et al. 2009). Since the initial implementation of HWRF in 2007, many systematic developments and upgrades have occurred within HWRF throughout the years (Bernardet et al. 2015). The latest release of the operational system (HWRF version 3.7a; Tallapragada et al. 2015) is configured with triply nested domains: the parent domain and two moving nested domains with 27, 9, and 3 km horizontal grid spacing, respectively. A vortex initialization procedure and a data assimilation system based on the Gridpoint Statistical Interpolation (GSI; Wu et al. 2002) are employed to optimize the storm-scale initial conditions for an HWRF forecast. Conventional observations and satellite observations restricted to clear-sky regions are assimilated into the intermediate domain. Satellite radiances are generally not assimilated in the innermost domain.

Both Tropical Rainfall Measuring Mission (TRMM, Simpson et al. 1996) and its successor, the Global Precipitation Measurement missions (GPM, Hou et al. 2014), provide remote observations of the Earth-atmosphere system. In addition, they also provide a relatively wide swath of data that is used to retrieve precipitation rates and information about the vertical structure of hydrometeors from the Goddard Profiling (GPROF) algorithm (Kummerow et al. 2001, 2015). Remote observations of precipitation characteristics can provide useful information about tropical cyclone development; in particular, precipitation structures like spiral bands and an eyewall that are concealed by a central dense overcast (Hence and Houze 2012); differentiating areas of non-

precipitating, stratiform precipitation, and convective precipitation. Assimilation of TRMM retrieved rain rates has been found to improve the forecast of tropical cyclone structure and precipitation (Pu et al. 2002; Hou et al. 2004; Kumar et al. 2014). Because GPM is relatively new (launched in 2014), there are few studies that have utilized GPM precipitation data for hurricane forecasts. Of the few studies, data assimilation techniques and strategies to assimilate GPM radiances affected by precipitation have been developed (Zupanski et al. 2011; Zhang et al. 2013; Chambon et al. 2014).

This study extends previous work by using the operational configuration of HWRF to include the capability to assimilate satellite retrieved precipitation data and to examine the impact in the inner-most domain of HWRF. There is a conceptual distinction between the assimilation of satellite *radiances* and the assimilation of *retrieved quantities* from satellite radiances. Satellite radiances are not assimilated in the innermost domain of HWRF; however, in this study, a retrieved quantity like hydrometeor profiles is assimilated in the innermost domain of HWRF.

To facilitate this effort, a newly developed variation of the GPROF algorithm called Hurricane GPROF (Brown et al. 2016) is used in this study. It utilizes observations from TRMM and GPM sensors to provide retrieved rain rates and hydrometeor profiles specifically for hurricanes. Those retrieved hydrometeor quantities are assimilated into HWRF. Since hydrometeor profiles from Hurricane GPROF are introduced into HWRF

for the first time, new observation operators are developed and implemented into the GSI data assimilation system within HWRF. Using these new capabilities, this study explores the impacts of assimilating satellite retrieved hydrometeor quantities in the innermost domain of HWRF.

This paper concentrates on results obtained from experiments with two Atlantic hurricanes, Hurricane Leslie (2012), and Hurricane Gonzalo (2014), and is organized as follows. An overview of the retrieved hydrometeors from TRMM and GPM, and the methodology of assimilating the Hurricane GPROF hydrometeor retrievals in HWRF are discussed in sections 2 and 3. Results from the experiments are presented in section 4; while section 5 details information related to the resulting HWRF forecasts. Finally, a summary and discussion along with some thoughts on future work are contained in section 6.

2. SATELLITE RETRIEVED HYDROMETEORS

2.1. TRMM and GPM Data

TRMM was launched in November 1997 to provide remote sensing of moderate to heavy rain events. Two principal precipitation measurement instruments on TRMM are the TRMM Microwave Imager (TMI) and the precipitation radar (PR). Precipitation retrievals are based on the emission of microwave radiation from raindrops that appears

warm against a cooler ocean background. After 17 years of service, the TRMM mission has come to an end in 2014. In February 2014, GPM was launched to continue, expand and improve the observations of global precipitation. There are two instruments that make up the GPM Core Observatory. One is the GPM Microwave Imager (GMI) and the other is the Dual-frequency Precipitation Radar (DPR). By including 4 channels whose frequencies are greater than 166 GHz, GMI is capable of retrieving a wide spectrum of precipitation intensities. Additional details of both TRMM and GPM are described in Kummerow et al. (1998) and Hou et al. (2014), respectively. Data from both platforms is used in hydrometeor retrievals.

2.2. Hydrometeor Retrieval

Several types of hydrometeor retrieval algorithms exist that could be used with TRMM and GPM observations. One type of algorithm that uses data from the corresponding precipitation radars on TRMM and GPM (PR and DPR, respectively) retrieves rain rates and vertical profiles of hydrometeors (e.g. Iguchi et al. 2000). However, a characteristic of the data from PR and DPR is that the swath width is generally smaller than a tropical cyclone. A second type of algorithm uses data from the corresponding imagers on TRMM and GPM (TMI and GMI, respectively) to retrieve rain rates and vertical profiles of hydrometeors. Unlike the relatively narrow swath width of both PR and DPR, the swath width of data from both TMI and GMI is large enough to observe the whole tropical cyclone. The second type of algorithm is referred to as the Goddard PROFiling

algorithm (GPROF; Kummerow et al., 2001); which to date is called GPROF 2014 (Kummerow et al., 2015). In addition, there is a customized retrieval algorithm for hurricane applications, referred to as Hurricane GPROF (Brown et al., 2016). Hurricane GPROF improves the GPROF 2014 retrievals in hurricane scenes by using a combination of 1) an empirical database that is developed from both PR and TMI, 2) best track information contained in HURicane DATa 2nd generation (HURDAT2; Landsea and Franklin 2013), and 3) GPROF 2014 retrievals are employed. Retrieved vertical profiles of hydrometeors from Hurricane GPROF are used in this study.

2.3. Preparation of Hurricane GPROF retrievals for Assimilation

Hurricane GPROF retrievals include vertical profiles of four hydrometeor types: 1) ice, 2) mixed-phase, 3) rain, and 4) cloud water (kg m^{-3}). In order to adjust for the capabilities of the HWRF modeling and data assimilation system, a decision is made to assimilate integrated values of vertical profiles of hydrometeors. This decision will likely produce better results because observation errors of vertical profiles are anticipated to be larger than the errors of the corresponding vertically integrated values. Assuming that errors of vertical profile are random and unbiased, as is normally done in data assimilation, it is likely that the sum of errors of a vertical profile will have cancellations due to errors with opposite signs, making the errors of integrated values smaller. In actuality, there are several possible sources of additional errors that are associated vertical profiles. The operational HWRF model has total cloud condensate (referred to as CWM) as prognostic

variable instead of individual hydrometeor types. If one would like to assimilate vertical profiles of hydrometeors with GSI, a procedure that converts CWM into individual hydrometeors types would have to be used, thus introducing additional errors. Another possible source of observation errors is the use of prescribed profiles in the Hurricane GPROF algorithm (Brown et al., 2016). All these factors suggest that assimilation of integrated values of hydrometeor profiles can be advantageous in this system.

Prior to vertical integration, four vertical profiles are transformed into two vertical profiles to simplify the data assimilation procedure. The two vertical profiles are solid condensate, referred to as solid-water content (SWC), and liquid condensate, referred to as liquid-water content (LWC). The SWC profile was made by adding values of the upper half of the mix-phased profile to the corresponding values of the ice profile; the LWC profile was made by adding values of the lower half of the mixed-phase profile to the corresponding values of the cloud and rain profiles. Finally, vertical integration was performed to yield an integrated value, one for SWC and one for LWC. Each of these values is then assimilated along with new observation operators.

3. METHODOLOGY FOR ASSIMILATING RETRIEVED INTEGRATED SWC AND LWC IN HWRF

3.1. NOAA Operational HWRF (2014 Implementation)

The HWRF version 3.6a (Tallapragada et al. 2014), which is functionally equivalent to the 2014 operational version of HWRF, is employed in this study. Modeling components in HWRF include 1) the Weather Research and Forecast model (WRF) software infrastructure, 2) the Nonhydrostatic Mesoscale Model (NMM; Janjic, 2003) dynamic core, 3) the Princeton Ocean Model for Tropical Cyclones (POM-TC; Yablonsky et al., 2015), and 4) the NCEP coupler which acts as an independent interface between the atmosphere and ocean components. Initialization portion of HWRF uses a vortex initialization package and the HWRF Data Assimilation System, which is a GSI based regional hybrid variational-ensemble data assimilation system.

There exist many options in the configuration of the operational HWRF. Some of the main options in the configurations are the Geophysical Fluid Dynamics Laboratory (GFDL) surface layer scheme, the GFDL slab land surface model, a modified GFDL long-wave and short-wave scheme, the modified Ferrier microphysics scheme for the tropics (Ferrier, 2005), the simplified Arakawa-Schubert (SAS) cumulus scheme, and the NCEP Global Forecasting System (GFS) boundary layer parameterization. Additional details of physics options in HWRF can be found in (Tallapragada et al. 2014).

In HWRF version 3.6a, the NMM core is configured with three domains and they are referred to as d01, d02, and d03. Those domains use a horizontal grid spacing of 27, 9, and 3 km, respectively. The size of domain 1 is about 5900 km x 5900 km; similarly, the

size of domain 2 is about 960 km x 960 km, and the size of domain 3 is about 600 km x 60 km, respectively (Fig. 1). Domain 3 is nested in domain 2, and domain 2 is nested in domain 1; furthermore, both d02 and d03 are storm-relative moving grids. Both inner nests are two-way interactive grids. To allow more observations to be assimilated in hurricane and its near environments, both d02 and d03 are extended to a larger size and they are referred to ghost d02 (about 1500 km x 1500 km) and ghost d03 (about 750 km x 750 km) (see Fig. 1). After GSI data assimilation, ghost d02 and ghost d03 are then interpolated back to the d02 and d03 domains as initial conditions for HWRF forecasts. There are 61 vertical levels and the model top extends to 2 hPa. The POM-TC is configured with a single trans-Atlantic ocean domain for North Atlantic basin and three-dimensional coupling for the east Pacific basin.

3.2. GSI and Vortex Initialization

HWRF data assimilation component utilizes GSI with a regional one-way hybrid ensemble-3DVar data assimilation scheme (Wang 2010). Background error covariance of the hybrid system is a combination of the static background error covariance embedded in GSI (Wu et al. 2002; Parrish and Derber 1992; Kleist et al. 2009) and the flow-dependent background error covariance estimated from the NCEP operational GFS 80-member ensemble forecast (T254L64) at a resolution of approximately 55 km. The static background error covariance is determined using the recursive filter (Purser et al. 2003) on the analysis grid, which is $\sqrt{2}\Delta x$ where Δx is the grid spacing of HWRF domains. In a

3DVar system, observations at different times are compared to only one background (also known as first guess) field. One optional aspect of GSI is to include additional background fields through the use of the First Guess at Appropriate Time (FGAT). FGAT is employed in GSI to assimilate observations over a time window by interpolating a time sequence of background fields to the actual observation times (Lorenc and Rawlins 2005). Currently, 3 background files that are valid at -3, 0, and +3 hours from the actual analysis time within a 6-h time interval are used. Control variables in the operational GSI include streamfunction, velocity potential, temperature, specific humidity, surface pressure, and ozone.

As part of the generation of a background field, the Global Data Assimilation System (GDAS) forecast is used. In addition to GDAS, either the storm vortex from a previous HWRF forecast or a bogus vortex will be used, depending upon the observed vortex intensity and the availability of a previous cycle that includes an HWRF forecast and an analysis. In the vortex initialization procedure, relocation, resizing, and intensity-correction were performed on the vortex based on the Tropical Cyclone Vitals Database (TCVitals[†]). More details of the vortex initialization process can be found in Tallapragada et al. (2014).

[†] TCVitals is an archive of Cyclone Message Files, which contain cyclone location, intensity, and structure information, created in real time by forecasting centers. Available online at http://www.emc.ncep.noaa.gov/mmb/data_processing/tcvitals_description.htm. These data are used to initialize tropical cyclone forecasts in several NCEP operational models via vortex bogusing and vortex relocation methods.

After vortex initialization, observations are assimilated by GSI. Observational data assimilated in GSI are categorized into conventional[‡] and satellite data. Satellite data assimilated in GSI includes both retrievals (including satellite derived winds and the GPS Radio Occultation data) and radiances. Satellite radiances can be categorized into clear-sky or cloudy sky. Currently, GSI assimilates clear-sky radiances from several geostationary and polar orbiting satellites. In operational setting, GSI data assimilation is performed within both ghost d02 and ghost d03. Conventional and satellite data are assimilated within ghost d02 while only conventional data is assimilated within ghost d03. This study extends the operational configuration by including satellite data assimilation within ghost d03 and exploring the usage of TRMM and GPM retrieved integrated SWC and LWC.

3.3. Observation Operators for Integrated SWC and LWC

In order to assimilate TRMM and GPM retrieved integrated SWC and integrated LWC, new observation operators (also known as a forward operator) along with the corresponding tangent linear and adjoint components are developed for this study. One possible choice of implementing the observation operators in this study would be to add hydrometeor mass mixing ratios to the current set of control variables. However, the

[‡] Conventional observations assimilated in operational GSI include radiosondes, dropwindsondes, aircraft reports, surface ship and buoy observations, surface observations overland, pibal winds, wind profilers, radar-derived Velocity Azimuth Display (VAD) wind, WindSat scatterometer winds, integrated precipitable water derived from the Global Positioning System (GPS). The NOAA P3 Tail Doppler Radar (TDR) radial winds are also assimilated in ghost d03 when they are available.

resulting changes in initial conditions of hydrometeors would have to be dynamically consistent with changes in the environment in initial conditions (such as temperature *T*, specific humidity *q*, and surface pressure *ps*), in order to support the existence of clouds/hydrometeors in the subsequent forecast. Such changes in the environment rely on cross-variable correlations between hydrometeor mass mixing ratios and the environment, defined by the background error covariance in the operational (i.e. hybrid) GSI. Unfortunately, the above-mentioned cross-variable correlations do not exist in the static background error covariance. On the other hand, the ensemble component of the background error covariance is obtained from the operational GFS 80-member ensemble forecasts (a model different from HWRF) that have relatively coarse resolution. In addition, the hydrometeor mass mixing ratios are set to zero during the vortex initialization procedure, implying that the background field is in clear sky condition. Although this could be avoided, it would require changes in the operational HWRF procedures (including vortex initialization and data assimilation). Due to the above-mentioned limitations, we choose to implement observation operators in such a way that the initial conditions that include *T, q,* and *ps* (used to infer three-dimensional pressure, *P*) are adjusted to support the existence of hydrometeors. The observations operators will be built under the operational configuration to extend the impact of assimilating integrated SWC and LWC to the current set of GSI control variables.

As part of the development of the new observation operators, the main assumption is that all water vapor in excess of the saturation is immediately condensed out (Cotton, 1972; Morrison et al., 2005; Thompson et al., 2004). The SWC and LWC of the retrievals are then approximated by the excess of saturation with respect to either ice or liquid water. The observation operator is then defined as a vertical integration of water vapor mixing ratio (kg kg^{-1}) in excess of saturation with respect to ice or liquid. However, such defined observation operator is likely to under-estimate the integrated water contents and thus leads to a negative bias of the background guess compared to the observed value. We will address this issue later.

Thus, the observation operator for integrated SWC, h_s, is

$$h_s = \begin{cases} \sum_{k=k_0}^{k_{max}} (q_v^k - q_{si}^k)\rho^k \Delta z^k & if \quad q_v^k \geq q_{si}^k \\ 0 & if \quad q_v^k < q_{si}^k \end{cases} \qquad (1)$$

where q_v is water vapor mixing ratio, q_{si} is saturation mixing ratio with respect to ice, Áis air mass density and can be inferred using *T, P, and* q_v, and z is layer thickness. The superscript k denotes the model vertical level index, k_0 is the vertical level where temperature is T_0 = 273.16 K, and k_{max} is the index for the top model level. Similarly, the observation operator for integrated LWC, h_l, is

$$h_i = \begin{cases} \sum_{k=1}^{k_{mix}} (q_v^k - q_{sl}^k)\rho^k \Delta z^k & if \quad q_v^k \geq q_{sl}^k \\ 0 & if \quad q_v^k < q_{sl}^k \end{cases} \quad (2)$$

where q_{sl} is saturation mixing ratio with respect to liquid, and k_{mix} is the vertical level where temperature is T_{mix} = 253.16 K.

Since specific humidity (q) is one of the control variables that will be updated in GSI, a conversion from specific humidity to water vapor mixing ratio, $q_v = \frac{q}{1-q}$, is required. In addition, the computation of saturation mixing ratio with respect to both ice and liquid will be required. This is done through the use of the following two equations:

$$q_{si} = 0.622 \frac{e_{si}}{P - e_{si}} \quad (3)$$

and

$$q_{sl} = 0.622 \frac{e_{sl}}{P - e_{sl}} \quad (4)$$

where e_{si} and e_{sl} are the saturation vapor pressure with respect to ice and liquid. In Eqs. (3) and (4), e_{si} and e_{sl} are only a function of temperature as described by the Clausius-Clapeyron equation[§]:

[§] For additional information about the Clausius-Clapeyron equation, the interested readers can refer to section 4.4 in (Emanuel 1994).

$$e_s(T) = P_0(\frac{T_0}{T})^{C_1} \exp[C_2(1-\frac{T_0}{T})] \quad (5)$$

where T_0 = 273.16 K, P_0 = 610.78 hPa, and two constants, C_1 and C_2. Both C_1 and C_2 are non-dimensional constants and have ice and liquid components, C_1^{ice}, C_1^{liquid}, C_2^{ice}, and C_2^{liquid} (see Table 1). As a result, the saturation vapor pressure with respect to ice and liquid can be expressed by

$$e_{si}(T) = P_0(\frac{T_0}{T})^{C_1^{ice}} \exp[C_2^{ice}(1-\frac{T_0}{T})] \quad for \quad T < T_{mix} \quad (6)$$

and

$$e_{sl}(T) = P_0(\frac{T_0}{T})^{C_1^{liquid}} \exp[C_2^{liquid}(1-\frac{T_0}{T})] \quad for \quad T > T_0 \quad (7)$$

In Eqs. (1) and (2), the observation operator for integrated SWC is applied for temperatures below T_0 and the observation operator for integrated LWC is applied for temperatures above T_{mix}. For temperatures within the interval (T_{mix}, T_0) where a mixture of SWC and LWC may exist, saturation vapor pressure is computed by linearly combining Eqs. (6) and (7):

$$e_s(T) = w \cdot e_{sl}(T) + (1-w) \cdot e_{si}(T) \quad (8)$$

where the weighting coefficient $w = (T- T_0)/(T_0 - T_{mix})$. Eqs. (6)-(8) and w together are used in GSI to compute saturation vapor pressure for three specific temperature ranges; $T < T_{mix}$, $T > T_0$, and $T_{mix} < T < T_0$. This three-equation formulation defines a piecewise

continuous function of temperature. Since temperature is one of the control variables in GSI, calculation of a temperature gradient during the cost function minimization process using the above-mentioned weight coefficient will likely introduce discontinuities at T_{mix} and T_0. To avoid discontinuities, an alternate version of the weighting coefficient is implemented, following (Zupanski 1993): $w = 0.5[1+tanh(\text{"}\,T)]$, where $\text{"}\,T = [T-0.5(T_{mix} + T_0)]/[0.25(T_0 - T_{mix})]$. As a result, a single equation, Eq. (8), with this new weighting coefficient is used to compute saturation vapor pressure for any given temperature. Eqs. (3) and (4) then become

$$\begin{cases} q_{si} \\ q_{sl} \end{cases} = 0.622 \frac{e_s(T)}{P - e_s(T)} \quad \begin{matrix} if \quad T < T_0 \\ if \quad T > T_{mix} \end{matrix} \qquad (9)$$

where e_s is computed by Eq. (8) and the new w. Equation (9) is then used in both observation operators h_s and h_l, Eqs.(1)-(2), in which both operators can be expressed as functions of the three variables that include T, P, and q.

In addition, the derivatives of the operator with respect to T, P, and q (often referred to as Jacobians) are also calculated and saved, implying that the tangent linear operator is a linear combination of perturbations of T, P, and q, in which Jacobians are the corresponding coefficients (see Appendix A). This also reduces the complexity of the adjoint operator, in which the same linear combination coefficients are used to compute gradients of perturbation in T, P, and q.

As described in Wang (2010), in hybrid GSI, covariance localization is conducted in the model space not in observation space as most ensemble data assimilation systems. The localization is applied to control variables in model grid space with prescribed correlation lengths. Therefore, no assumption about the explicit position of the observation is required during the procedure of the covariance localization.

Due to the introduction of new observation types (integrated SWC and integrated LWC) and new observation operators, Eqs. (1)-(2), into the operational HWRF GSI system, single observation (1-OBS) experiments are conducted. The 1-OBS experiments are conducted to examine the influence of assimilating retrieved integrated SWC and integrated LWC on some of the state variables in GSI within a hurricane environment.

3.4. 1-OBS Experiments

Two sets of two 1-OBS experiments are performed with an HWRF simulation of Hurricane Leslie (2012)[**]. The first set of experiments include 1-OBSSOLID and 1-OBSLIQUID, where a single observation of integrated SWC and integrated LWC with value of 0.5 kg m^{-2} is placed at 21.8^{o}N, 60.0^{o}W, about 150 km east of the center of Leslie at 1800 UTC 2 September. The background guessed value of integrated SWC and integrated LWC at this location is 0.001 kg m^{-2} and 0 kg m^{-2}, respectively. The

[**] Additional details about Hurricane Leslie (2012) are provided in a subsequent section.

observation error is 0.5 kg m^{-2} for both integrated SWC and LWC observations. In the first set of experiments, GSI is performed without the hybrid option (i.e. static background error covariance only). Thus, the analysis from the first set of experiments represent results from a 3DVar assimilation. Similarly, the second set of experiments also includes 1-OBSSOLID and 1-OBSLIQUID. However, GSI is performed with the hybrid option (i.e. GFS ensemble forecasts is utilized in the background error covariance). Analyses from the second sets of experiments represent outputs from an ensemble-3DVar assimilation. Results from these 1-OBS experiments highlight the influence of the integrated SWC and integrated LWC on state variables through the use of the new observation operators and background error covariance (Parrish and Derber 1992). Visualization of the results will be shown by using an analysis increment (analysis minus background) from the 1-OBS experiments.

To begin with, output from both the 1-OBSSOLID and the 1-OBSLIQUID experiments neglecting the hybrid option is described. The analysis increments from 1-OBSSOLID are presented in an east-west vertical cross-section along the latitude of the location of the single observation that is 21.8^{o}N as shown in Figs. 2a-b and d. Values of the analysis increment in *T* are negative with a local minimum of about -0.02 K near 60^{o}W and 400 hPa; implying a reduction of the values of the temperature in the analysis. A local maximum of about 0.024 g kg^{-1} near 60^{o}W and 500 hPa in the analysis increment of *q* is evident in Fig. 2b; suggesting an increase of the values of *q* in the analysis field. Fig. 2c,

which shows the analysis increment of the *ps* indicates an increase in the values of the analysis increment of *ps*; consequently, values of *ps* in the 1-OBSSOLID analysis increase. Fig. 2d shows the response of the analysis increment of the v-component of the wind field to the inclusion of the integrated SWC. Similarly, Figs. 2e-f and h, present the analysis increments from 1-OBSLIQUID in the same east-west cross-section as Figs. 2a-b and d. Values of the analysis increment in *T* are negative with a local minimum of about -0.016 K near 60^{o}W and surface; implying a reduction of the values of the temperature in the analysis. A local maximum of about 0.09 g kg^{-1} near 60^{o}W and surface in the analysis increment of *q* is evident in Fig. 2f; suggesting an increase of the values of *q* in the analysis. Fig. 2g exhibits a decrease in the values of the analysis increment of *ps*; consequently, values of *ps* in the 1-OBSLIQUID analysis decrease. Response of the analysis increment of the v-component wind field to the inclusion of the integrated LWC is illustrated in Fig. 2h.

A reasonable physical interpretation is possible for these no-hybrid experiment results. Note that the *q* increments are positive in both Figs. 2b and f in response to increased observation innovation. Similarly, the *T* increments are negative in both Figs. 2a and e in response to approaching saturation with respect to ice/liquid water. In sharp contrast, the *ps* increments are of opposite signs in Figs. 2c and g. At first, such a result may seem contradictory. Resolution of the apparent contradiction may be provided through the use of the integrated form of the hydrostatic equation that can be expressed as:

$$P(z_l) = P(z_u) \cdot \exp[\frac{g(z_u - z_l)}{R_d \overline{T_v}}] \quad (10)$$

where z_u and z_l are the upper and lower physical heights, g is the acceleration due to gravity, R_d is the dry gas constant, and T_v is the averaged virtual temperature in a layer between z_u and z_l. That is, the simulated atmosphere in the no-hybrid experiments is assumed to be in hydrostatic balance. The key variable to focus on in eq. (10) is the virtual temperature: $\overline{T_v} = T(1 + 0.6 \cdot q_v)$.

Note that $\overline{T_v}$ is a function of not only T, but also q_v. Consider the negative values of the T analysis increments (Fig. 2a), they imply a decrease in T. By itself, a T decrease will act to decrease $\overline{T_v}$. Although there is a positive analysis increment of q (Fig. 2b; equivalent to a positive increment in q_v because $q_v = \frac{q}{1-q}$), values of q in the analysis are too small to offset the influence of T on $\overline{T_v}$. Therefore, values of $\overline{T_v}$ in the analysis decrease. Since $\overline{T_v}$ exists in the denominator in eq. (10), the argument of the exponent increases, leading to an increase in *ps* (Fig. 2c). In the lower troposphere, values of q can be approximately two orders of magnitude larger than those in the upper troposphere. As a result, relatively larger values of q in the lower troposphere can offset the influence of a T decrease on $\overline{T_v}$ (as inferred by Figs. 2e-f), resulting in an increase in $\overline{T_v}$. An increase in $\overline{T_v}$ causes the argument of the exponent in eq. (10) to increase, thus reducing *ps* (Fig. 2g). The above

analysis therefore provides a resolution to the apparent contradiction. In addition, wind adjustment (Figs. 2d and h) can be understood via the mass-wind balance relationships prescribed in static background error covariance embedded in GSI (e.g. Parrish and Derber 1992).

We now move on to results obtained when the hybrid option is used. In the hybrid experiments, the background error covariance is comprised of a linear weighting of 20% of the static 3DVar error covariance that is embedded in GSI and 80% of the error covariance that originates within the GFS 80-member ensemble forecasts. This linear weighting follows the operational configuration of GSI. Thus, analysis increments from the hybrid experiments are expected to show a blended influence from both the static and flow-dependent background error covariance.

The region containing the dominant impacts in the hybrid experiments extends vertically through a significant portion of the simulated troposphere (Fig. 3). In general, the response to the analysis increments of the above mentioned fields in the hybrid experiments exhibits more spatial variability compared to the no-hybrid experiments. In addition, the magnitudes of the analysis increments are larger than the corresponding analysis increments from the no-hybrid experiments. While both no-hybrid and hybrid experiments assimilated the same observation and used the same observation operator, the only difference between the no-hybrid and hybrid experiments is through the use of a

flow-dependent ensemble background error covariance. The difference is likely due to the cross-correlation (or cross-covariance) that is described differently between the static and ensemble background error covariance. Cross-correlation contains information about the relationship between different state variables. By giving a larger weight on the ensemble background error covariance (80%), the dominant responses to analysis increments are expected to mostly come from the ensemble component.

Interestingly, the dominant negative increments in T near 61 ^{o}W and between 500 hPa and surface (Fig. 3a) are approximately collocated with the positive increments in q (Fig. 3b), suggesting lowering temperature and increasing moisture together to approach saturation. Similar collocated increments in T and q near 61 ^{o}W and between 700 hPa and surface are evident in Figs. 3e and f. In addition, negative ps increments and dipoles of opposite signs of v increments (Figs. 3c-d and g-h) show deepened surface pressure accompanied by enhanced low level cyclonic flows in a physically consistent way. Although a concise physical interpretation is more challenging for the hybrid experiments, analysis increments of the four variables exhibit an adjustment from a background state to an analysis in a consistent way. These results, along with the no-hybrid experiments, suggest that the new observation operators are extending the impacts of assimilating new observations to the state variables in a physically consistent manner.

4. DATA ASSIMILATION EXPERIMENTS

4.1. Case Description

Both Hurricane Leslie (2012) and Gonzalo (2014) were long-lived and spent the majority of their lives in the Atlantic Ocean without making landfall at the continental U.S. Their long lives allow sufficient TRMM and GPM observations to be collected. The detailed descriptions of these cases follow.

4.1.1. HURRICANE LESLIE

Leslie was a Category 1 hurricane that spanned the period from 30 August to 12 September 2012. Leslie developed from a tropical wave moved off the west cost of Africa, and strengthened into a tropical depression near the northern Leeward Island around 30 August 2012. After acquiring tropical storm status, Leslie moved steadily west northwestward and slowly intensified by September 2. A high-latitude blocking pattern over Atlantic Canada resulted in weak steering currents that caused Leslie to drift slow for four days. It was later upgraded to Category 1 hurricane with maximum sustained wind speed of 65 kt at 0600 UTC on September 5 due to the weakened deep-layer shear (Stewart, 2013). Visible satellite image from the Geostationary Operational Environmental Satellite-13 (GOES-13) shows Leslie at its peak intensity, 70 kt at 1145 UTC 5 September 2012 (Fig. 4a).

4.1.2 HURRICANE GONZALO

Gonzalo spanned the period of 12-20 October 2014. It was the strongest hurricane in the Atlantic since hurricane Igor (2010). Unlike Leslie, Gonzalo became a tropical storm east of Antigua by 1200 UTC 12 October 2014 and quickly strengthened into a hurricane within 1 day. Gonzalo then turned west northwestward and made landfall on Antigua, St. Martin and Anguilla as Category 1 hurricane at 1200 UTC on October 13, causing damages to those and nearby islands. Shortly thereafter, Gonzalo moved northwestward as it rapidly intensified into a Category 4 major hurricane by 0000 UTC October 15 (Brown, 2015). The maximum sustained wind of 125 kt was observed at 1200 UTC 16 October when Gonzalo reached its peak intensity. Fig. 4b shows Gonzalo in a visible image at 1145 UTC 16 October.

4.2. Experimental Design

Two data assimilation experiments are designed (Table 2) to evaluate the assimilation of Hurricane GPROF retrieved integrated SWC and LWC in the innermost domain of HWRF and they are as follows:

(i) The control experiment (denoted by CTL) uses the 2014 HWRF operational configuration (i.e. hybrid option of GSI and other features mentioned in sections 3.1 and 3.2) that assimilates both conventional and satellite observations in ghost d02. In ghost d03, however, only conventional observations are assimilated.

(ii) The second experiment (denoted by AddWC) is the same as (i). In addition to conventional observations, integrated SWC and LWC retrieved from Hurricane GPROF are also assimilated in ghost d03.

Both the CTL and the AddWC experiments are conducted for Hurricane Leslie (2012) and Hurricane Gonzalo (2014), respectively. Hurricane GPROF retrieved integrated SWC and LWC from TRMM are available near 0000 and 1800 UTC for Leslie. To assimilate the available retrievals in the 6-hour cycling of GSI, HWRF is initialized on 1800 UTC and cycled through 0000 UTC of the next day for Hurricane Leslie (2012).

Similarly, Hurricane GPROF retrieved integrated SWC and LWC from GPM for Hurricane Gonzalo (2014) are available near 0600 and 1200 UTC, and occasionally near 0000 UTC. To be consistent with the experimental design for Leslie, the first cycle for Gonzalo starts at 0600 UTC with the second cycle on 1200 UTC. If there is no Hurricane GPROF retrieved observations available on 1200 UTC, the first cycle will be starting at 0000 UTC with the second cycle on 0600 UTC.

Due to the data availability mentioned above, only two consecutive cycles that assimilate the Hurricane GPROF retrievals are conducted for both Gonzalo and Leslie.

Note that for all the AddWC experiments mentioned above, the observation errors assigned to integrated SWC and LWC are 1.0 and 2.0 kg m^{-2}, respectively. These two numbers are estimates of a root-mean-square deviation from all available Hurricane GPROF retrieved quantities for Leslie and Gonzalo. With this error assignment, the ratio of observation errors to the mean value of observed quantities is approximately 0.25 for integrated SWC and 0.4 for integrated LWC.

There are a total of six experiments. The first pair of experiments is conducted for Leslie, hereafter denoted by L1 CTL and L1 AddWC. In both L1 experiments, the first cycles begin at 1800 UTC 30 August and continue to the second cycles at 0000 UTC 31 August. Similarly, a pair of experiments is conducted during the observed developing stage of Gonzalo and is denoted by G1 CTL and G1 AddWC. In both G1 experiments, the first cycles begin at 0000 UTC 13 October and continue to the second cycles at 0600 UTC on the same day. During the observed mature stage of Gonzalo, the last pair of experiments is conducted and is denoted by G2 CTL and G2 AddWC. Likewise, in both G2 experiments, the first cycles begin at 0600 UTC 16 October and continue to the second cycles at 1200 UTC on the same day. The above-mentioned six experiments are summarized in Table 3.

Since the main difference between the CTL and AddWC experiments occur in the innermost domain, a discussion of the performance of the subsequent analysis from the second cycles of the six experiments will be specific to d03.

4.3. Results from Data Assimilation Experiments

4.3.1 OBSERVED VS. SIMULATED INTEGRATED SWC AND LWC

In general, background guessed values of the observed quantities are lower, potentially suggesting a negative bias due to the observation operators. An example of the observed integrated SWC and LWC that are assimilated in ghost d03 in the L1 AddWC experiment is shown in Figs. 5a-b. The background guessed values of integrated SWC and LWC and the counterpart from the analysis are illustrated in Figs. 5c-d and Figs. 5e-f, respectively. Before assimilation, the local maximum values (~ 2.5 kg m^{-2}) of the observed integrated SWC (Fig. 5a), to the southwest quadrant of the storm (magenta star), are found to be lower in the background (Fig. 5c). Similar remarks also apply to the integrated LWC (see Figs. 5b and d). By assimilating the observed integrated SWC and LWC together with the new observation operators, background guessed values of the integrated SWC and LWC are improved (Figs. 5e and f) and are supported by values of the observed quantities (Figs. 5a and b). When observed quantities for Gonzalo are assimilated into the G1 AddWC (Figs. 6a and b) and G2 AddWC (Figs. 7a and b) experiments, favorable results occurred in that observed quantities support the subsequent analyses. Results from L1, G1, and G2 AddWC experiments (Figs. 5-7) are encouraging as they add confidence of

the ability of the new observation operators (see section 3.3) that serve to modify background state into an analysis state that agrees with observations. Although there is still an indication of the potential bias, the observation innovation is considerably reduced in the analysis.

4.3.2 DIFFERENCES BETWEEN THE CTL AND ADDWC ANALYSES

As a result of the assimilation of retrieved integrated SWC and LWC in ghost d03 (AddWC experiment), the impact of the additional observations on the respective analyses (CTL vs. AddWC) is examined. Instead of taking difference between the background and analysis fields of one experiment (analysis increment, as was done in section 3.3), differences between analyses from the CTL and AddWC experiments are examined here. Due to possible asymmetries, in the azimuthal direction, a given vertical cross-section could contain information that may or may not be representative of the entire hurricane. To overcome this issue, azimuthally-averaged quantities will be used to show differences between the two analyses, following Wu et al. (2014). To aid this analysis, horizontal winds in the rectilinear coordinate system (u and v) are converted to radial (V_r) and tangential (V_t) horizontal winds in a polar coordinate system centered on the hurricane.

Analyses of the L1 CTL and the L1 AddWC and the differences (L1 AddWC minus L1 CTL) are presented in Fig. 8. Values of azimuthally-averaged T, q, V_t, and V_r from the L1

CTL analysis are shown in Figs. 8a-d. Likewise, Figs. 8e-h show the four above variables from the L1 AddWC analysis. To examine the impact of assimilating both retrieved integrated SWC and LWC, differences between the two respective analyses are presented in Figs. 8i-l. In Fig. 8i, a local area of negative values of T differences between 300 and 800 hPa within the first 300 km radius suggests cooler air in the mid tropospheric layers of the L1 AddWC analysis. Positive values of q difference (Fig. 8j) are collocated with the negative T differences in Fig. 8i, suggesting cooler air in the mid tropospheric layers is accompanied by moister air. Negative values of V_t differences (Fig. 8k) and positive values of V_r differences (Fig. 8l) near surface and outside the first 50 km radius imply weaker rotational winds and inflows in the lower tropospheric layers of the L1 AddWC analysis. In contrast, large positive values of V_t differences (Fig. 8k) and positive values of V_r differences (Fig. 8l) above 300 hPa both suggest stronger rotational winds and outflows in the upper tropospheric layers of the L1 AddWC analysis. The impact of assimilating both retrieved integrated SWC and LWC in the core region of Leslie on the above-mentioned variables are mixed. Thus, physical interpretations are precluded. In general, moister and cooler air in near core region is evident in the mid tropospheric layers of the L1 AddWC analysis, suggesting a favorable environment for saturation. Slightly weaker winds in lower, but much stronger upper layer rotational winds and outflows are also evident in the L1 AddWC analysis.

Similar to Fig. 8, azimuthally-averaged quantities from the G1 CTL and G1 AddWC analyses and the difference fields are shown in Fig. 9. While responses to T are mixed (Fig. 9i), moister air throughout the vertical column within the first 100 km radius is evident in the G1 AddWC analysis (Fig. 9j). In Figs. 9k and l, V_t and V_r differences both suggest the G1 AddWC analysis has slightly stronger rotational winds throughout the vertical, and also greater inflows in the lower layer and greater outflows in the upper layer compared to the G1 CTL analysis. In general, large spatial variability in the difference fields is evident. Such a response is expected due to the mixed impact from assimilating both retrieved integrated SWC and LWC with the hybrid option (i.e. the operational configuration of GSI in HWRF). Like the 1-OBS hybrid experiments, physical interpretation of analysis differences is challenging. Since our cases are hurricanes, one approach could be to examine the hydrostatic linking of warmer temperatures aloft with lower surface pressures (as was described in section 3.4) to larger tangential wind speeds through gradient wind balance. However, for the simulations presented herein, azimuthally-averaging (e.g. Figs. 8 and 9) removes asymmetries that are present in the three-dimensional analysis fields. For brevity, conclusions from the G2 experiments are similar to G1.

Overall, results from the six experiments are encouraging. By assimilating additional observations in ghost d03 (AddWC experiments), background guessed values of the integrated SWC and LWC are adjusted to an analysis state that is supported by observed

quantities. In general, the impact of assimilating both retrieved integrated water contents causes moister and cooler air in the mid tropospheric layers to approach saturation when background guess values are lower (e.g. Figs. 5-7). While responses to the winds are mixed, results indicated increased rotational and radial winds in the upper layers.

5. HWRF FORECAST

A variety of metrics will be used to examine the impact of assimilating Hurricane GPROF data on HWRF forecasts. To begin with, hurricane track, size[††], and intensity of six forecasts are computed by using the GFDL vortex tracker (Marchok, 2002) package embedded in HWRF. These metrics are then compared with the NHC best-track data. Also, simulated precipitation fields from all six forecasts are compared with rain rates from the TRMM and GPM instruments. Finally, synthetic GOES-13 images generated from all six forecasts (using a version of CRTM external to HWRF) are compared with observed GOES-13 images (e.g., Grasso et al. 2014).

5.1. Hurricane Track, Size, and Intensity

Hurricane track, size, minimum central sea level pressure (MSLP), and maximum 10-m winds (WMAX) from two 126-h HWRF forecasts that are initialized with L1 CTL (blue line) and L1 AddWC (green line) analyses are presented in Fig. 10. Results show that

[††] Hurricane size is often described by the maximum extent of winds of 34, 50, and 64 kt in each of quadrants about the center (Landsea and Franklin 2013). In this study, quadrant averaged 34 kt wind radius is used as an approximation of hurricane size.

there is no obvious difference between track forecasts from L1 CTL and L1 AddWC (Fig. 10a). On the other hand, both L1 CTL and L1 AddWC forecasts generate larger storms (~100 km larger than the NHC best-track data), and remain larger than the NHC (black line) estimated sizes for the first 36 hours (Fig. 10b). Similarly, the intensity as measured by MSLP and WMAX of the simulated storms from the L1 CTL and the L1 AddWC forecasts produce more intense storms than the NHC estimates (Figs. 10c and d). Note, in particular, the L1 AddWC forecast however, intensifies the simulated hurricane after the first 72 hours and is much different than the L1 CTL forecast.

Fig. 11 shows results from the G1 CTL (blue line) and the G1 AddWC (green line) forecasts are presented in. Similar to the L1 Leslie forecasts, Fig. 11a exhibits no obvious distinction between the G1 CTL and the G1 AddWC track forecasts. In this case, the simulated storm sizes from both forecasts are found to be comparable to the NHC estimated sizes (black line) in the first 18 hours of the forecasts (Fig. 11b). However, the difference in sizes between both G1 forecasts and the NHC estimated sizes is nearly constant with a value of ~ 20 km, indicating slightly larger storm sizes in both forecasts. Unlike the L1 forecasts, values of MSLP and WMAX (Figs. 11c and d) suggest both G1 CTL and G1 AddWC forecasts underestimate the intensity of Gonzalo when compared to the NHC estimates throughout the 126-hour period. It is noteworthy that the G1 AddWC intensity forecast is generally better than the G1 CTL intensity forecast.

As for the last pair of forecasts, results from the G2 CTL and G2 AddWC are presented in Fig. 12. Both track and size comparisons from the G2 CTL and G2 AddWC forecasts exhibit similarities to the previous two pairs of forecasts (Figs. 12a and b). Unlike the L1 and G1 pairs of forecasts, the G2 pair of forecasts is initialized at a time when Gonzalo was a hurricane and covers the time period when the system underwent continuous weakening, underwent extra-tropical transition (completed on 19 Oct 18 UTC, 78 h), and eventually dissipated. In Figs. 12c and d, the G2 CTL and G2 AddWC forecasts of MSLP are found to be quite similar to the NHC estimated intensity for the first 48 hours. In the rest of the forecast period, MSLP forecasts from both G2 CTL and G2 AddWC exhibit relatively large deviation from the NHC estimates during the period of extra-tropical transition; however, the corresponding WMAX forecasts are rather similar to the NHC estimated quantities.

5.2. Precipitation

Simulated precipitation fields from all six forecasts are compared with rain rates from TRMM and GPM instruments. For this study, footprint sizes of instantaneous rain rates (mm hr^{-1}) from TRMM at nadir are ~30 x 20 km^2 and ~4.3 km for TMI and PR, respectively. Similarly, footprint sizes of instantaneous rain rates (mm hr^{-1}) from GPM at nadir are ~16 x 10 km^2 and ~5 km for GMI and DPR, respectively. In addition, d03 is small enough that the hurricane rainbands extend beyond the boundary of the innermost domain; consequently, simulated and observed rain rates will be displayed in d02. Due to

the footprint sizes of rain rate data from TRMM/GPM, a comparison of patterns near the cumulus scale is avoided in favor of a qualitative comparison of patterns on a larger scale.

Although instantaneous rain rates are unavailable from HWRF, other output variables are used to compare with TRMM/GPM. One such variable is the total cloud water condensate (kg kg^{-1}; referred to as CWM). Following Zhang et al. (2013), CWM is integrated over the depth of the simulated domain and is displayed in Fig. 13.

Rain rates from TMI/PR that are valid at 1800 UTC 31 August 2012 are compared to the column-integrated CWM field (kg m^{-2}; equivalent to mm) from the L1 CTL and the L1 AddWC 18-h forecasts (Figs. 13a-c). Like observations (Fig. 13a), the majority of the precipitation field is to the south of the center of Leslie (bold star) in both the L1 CTL (Fig. 13b) and the L1 AddWC (Fig. 13c) forecasts. Larger values of column-integrated CWM to the south of the simulated systems are reminiscent of convective activity that advects cyclonically around the center. Similar to the L1 forecasts, the simulated rain rates from both G1 forecasts exhibit larger values to the northeast of the center of Gonzalo (bold star) and are supported by observed rain rates from GMI/DPR (Figs. 13d-f). Unlike the spatial patterns exhibited in Figs. 13a-f, the regions of simulated rain rates encircle the center of Gonzalo (bold star) in both observed and simulated fields (Figs. 13g-i). Similar comparisons between simulated rain rates from HWRF forecasts and

retrieved rain rates from the Advanced Microwave Sounding Unit were also examined and showed similar results, but were not shown for the sake of brevity.

5.3. Synthetic Satellite Images

Due to the lack of available observations over oceans, TRMM/GPM rain rates are supplemented with GOES-13 images. One way to use observed GOES-13 images is through the use of satellite images generated from HWRF outputs (referred to as synthetic satellite images). Synthetic satellite images (Bikos et al. 2012) for all six forecasts are shown along with observed GOES-13 images at 10.7 μm (Fig. 14). In the figure, observed and synthetic GOES-13 imagery from the L1 CTL and the L1 AddWC forecasts are shown in Figs. 14a-c; imagery from the G1 CTL and the G1 AddWC forecasts are exhibited in Figs. 14d-f; and results from the final pair are displayed in Figs. 14g-i. All synthetic images are generated with the CRTM and brightness temperatures are sensitive to particle sizes. For this study, particle size of ice is set to 75 μm; a size that is consistent with particle sizes of ice in GSI.

In general, the area within the dash boxes of the synthetic images that is occupied by cold clouds (< -60^{o}C) is larger than the corresponding area in the observed images. These cold biases are particularly evident in the coldest cloud tops with HWRF forecasts having nearly twice as much area being covered by cloud tops colder than -70^{o}C. It is interesting to note that as the temperature threshold is increased to -40^{o}C the areal coverage in

HWRF is more comparable and actually slightly smaller than the observations. This may be suggesting that the convective vertical motions are over active in HWRF or other issues related to microphysics. Additionally, these findings are consistent with observational studies relating IR imagery to tropical cyclone wind structures (Knaff et al. 2014, Knaff et al. 2015) and the results presented in section 5.1, in which a larger and more intense tropical system is found in both L1 CTL and L1 AddWC forecasts. Finally, it is also noteworthy that the assimilation of retrieved integrated SWC and LWC from TRMM/GPM provides slightly improved initial conditions in terms of the observed GOES-13 imagery.

6. SUMMARY AND DISCUSSION

The GSI capability of assimilating satellite retrieved integrated SWC and LWC from Hurricane GPROF in HWRF is developed and assessed in this study. To assimilate the retrieved integrated water contents, new observation operators are developed and implemented in GSI. The concept behind the development of the new observation operators assumes all water vapor in excess of saturation with respect to ice or liquid will be immediately condensed out. Without introducing new control variables into GSI, the new observation operators are implemented in such a way that the information of integrated water contents is extended to some -- temperature, specific humidity and pressure -- of the current set of GSI control variables.

Two 1-OBS experiments that use the no-hybrid option are conducted to assimilate a single integrated SWC and a single integrated LWC both of which are for a hurricane environment. Both no-hybrid experiments suggest that the new observation operators are capable of extending information from integrated SWC and integrated LWC into nearby grid points and other state variables in a physically consistent way. In particular, a concise physical interpretation is provided to explain analysis increments in temperature, specific humidity, and surface pressure from the no-hybrid 1-OBS experiments. Results from the corresponding experiments that are conducted with a hybrid option exhibit more spatial variability because of the inclusion of flow-dependent background error covariance that originate from GFS ensemble forecasts. Due to the variability in the hybrid 1-OBS experiments, a physical interpretation is less straightforward. Nevertheless, analysis increments from the above mentioned state variables exhibit consistent adjustment from a background state to an analysis.

Two hurricanes, Leslie (2012) and Gonzalo (2014), are selected to perform three sets of two data assimilation experiments with the use of the retrieved integrated SWC and LWC within HWRF. A CTL experiment, following the current operational HWRF implementation, and an AddWC experiment that assimilates Hurricane GPROF retrieved integrated SWC and LWC together along with conventional observations in the innermost domain are conducted. In general, moister and cooler air in mid to lower tropospheric layers of the hurricane core are evident in AddWC analysis, suggesting a

tendency toward reaching saturation by lowering temperature and increasing moisture. Tangential and radial winds resolved in the AddWC analysis are slightly more intense in the mid to upper tropospheric layers, near the hurricane core, compared to the CTL analysis.

Although "all water vapor in excess of the saturation is immediately condensed out" is a valid assumption, the model microphysics and/or cumulus parameterization has already condensed out a portion of super-saturated water vapor. As a result, the super-saturation computed by the observation operators is likely reduced, therefore potentially creating a negative bias of the guess. A possible remedy for this issue will be to introduce/add a model variable in HWRF to retain an adequate amount of excessive water vapor. Nevertheless, the results indicate that the system is still able to considerably reduce the observation innovation in the analysis.

In general, the impact of assimilating the TRMM/GPM precipitation observations (integrated SWC and integrated LWC) in the innermost domain on the HWRF forecasts is inconclusive. Both the CTL and the AddWC forecasts generate larger hurricanes compared to observations. However, the impact on the AddWC forecasts was to produce lower MSLP and greater WMAX at times. Comparisons between both the CTL and the AddWC forecasts to TRMM/GPM rain rates suggest that the simulated precipitation fields are not only similar between the two forecasts, but also comparable to

observations. The synthetic satellite images generated from the CTL and the AddWC forecasts exhibit similar characteristics. However, issues in the synthetic images are identified from a comparison between synthetic and observed GOES-13 images. These issues include 1) colder cloud top brightness temperatures and 2) larger spatial extension of cold brightness temperatures, both in the vicinity of the simulated tropical storms. A few possible causes of the inconclusive nature of our results are the following: 1) the analysis used to initialize an HWRF forecast is unbalanced, 2) the existence of forecast model errors (e.g. errors in microphysics parameterization schemes) that are not accounted for by the HWRF data assimilation system, and 3) the absence of hydrometeor variables in the list of operational GSI control variables.

A few different approaches will be explored in future work. In this study, a retrieved quantity was assimilated and the impact on HWRF forecasts was inconclusive. A statistical inference about the impact on the general population of experiments where retrieved precipitation observations are assimilated into HWRF requires more experiments than the two presented here (i.e., sample size is too small). Long-term efforts will extend current work by conducting similar experiments with more hurricane cases and also explore the feasibility of assimilating all-sky satellite radiances directly into HWRF.

Acknowledgements

This research is primarily funded by NOAA's Sandy Supplemental Award Number NA14OAR4830122. We would like to acknowledge the high-performance computing support from Yellowstone provided by NCAR's Computational and Information Systems Laboratory, sponsored by the National Science Foundation. The views, opinions, and findings in this report are those of the authors, and should not be construed as an official NOAA and or U.S. Government position, policy, or decision.

APPENDIX A. JACOBIANS FOR INTEGRATED SWC AND INTEGRATED LWC OPERATORS

The derivatives of the integrated SWC and/or integrated LWC operator with respect to *T*, *P*, and *q*, also known as Jacobians, are also calculated. From Eqs (1)-(9), the operator at each model vertical level *k* can be re-written as

$$h^k = \left[\left(\frac{q^k}{1-q^k} \right) - 0.622 \frac{e_s(T^k)}{P^k - e_s(T^k)} \right] \rho^k \Delta z^k \quad \text{(A1)}$$

using the same notations. Since $\rho^k \Delta z^k$ is equivalent to $\frac{\Delta P^k}{g}$ according to the hydrostatic equation and ideal gas law, Eq. (A1) can be written as

$$h^k = \left[\left(\frac{q^k}{1-q^k} \right) - 0.622 \frac{e_s(T^k)}{P^k - e_s(T^k)} \right] \frac{\Delta P^k}{g} \quad \text{(A2)}$$

For simplicity, the vertical index *k* is dropped, and the operator at each model vertical level can then be expressed by

$$h = \left[\left(\frac{q}{1-q} \right) - 0.622 \frac{e_s(T)}{P - e_s(T)} \right] \frac{\Delta P}{g} \quad \text{(A3)}$$

as a function of *T*, *P*, and *q*: $h = f(T, P, q)$

The corresponding tangent linear and adjoint operators are a linear combination of perturbations of *T*, *P*, and *q*:

$$\delta h = \frac{\partial h}{\partial T} \delta T + \frac{\partial h}{\partial P} \delta P + \frac{\partial h}{\partial q} \delta q \quad \text{(A4)}$$

where ′*h* represents the increments of integrated SWC or integrated LWC, and ′*T*, ′*P*, and ′*q* are the perturbations of *T*, *P*, and *q*, respectively. Similarly, $\frac{\partial h}{\partial T}$, $\frac{\partial h}{\partial P}$, and $\frac{\partial h}{\partial q}$ are the Jacobians with respect to *T*, *P*, and *q*. Based on the approximate calculation of derivatives of $\frac{\Delta P}{g}$ with

respect to T, P, and q, it is assumed that these derivatives are negligible compared to the derivatives of $(\frac{q}{1-q})-0.622\frac{e_s(T)}{P-e_s(T)}$ with respect to T, P, and q. The Jacobians can then be written as below:

$$\frac{\partial h}{\partial T}=-0.622\frac{P}{(P-e_s)^2}\frac{\partial e_s}{\partial T}\frac{\Delta P}{g} \quad \text{(A5.1)}$$

$$\frac{\partial h}{\partial P}=0.622\frac{e_s}{(P-e_s)^2}\frac{\Delta P}{g} \quad \text{(A5.2)}$$

$$\frac{\partial h}{\partial q}=\frac{1}{(1-q)^2}\frac{\Delta P}{g} \quad \text{(A5.3)}$$

In Eq. (A5.1),

$$\frac{\partial e_s}{\partial T}=e_{sl}\frac{\partial w}{\partial T}+w\frac{\partial e_{sl}}{\partial T}-e_{si}\frac{\partial w}{\partial T}+(1-w)\frac{\partial e_{si}}{\partial T} \quad \text{(A6)}$$

where

$$\frac{\partial w}{\partial T}=2\frac{1}{\cosh^2(\Delta T)}(\frac{1}{T_0-T_{mix}}) \quad \text{(A7)}$$

$$\frac{\partial e_{sl}}{\partial T}=e_{sl}(\frac{-C_1^{liquid}}{T}+C_2^{liquid}\cdot\frac{T_0}{T^2}) \quad \text{(A8)}$$

and

$$\frac{\partial e_{si}}{\partial T}=e_{si}(\frac{-C_1^{ice}}{T}+C_2^{ice}\cdot\frac{T_0}{T^2}) \quad \text{(A9)}$$

The above equations are implemented in GSI.

References

Bernardet, L., and Coauthors, 2015: Community Support and Transition of Research to Operations for the Hurricane Weather Research and Forecasting Model. *Bull. Am. Meteorol. Soc.*, **96**, 953–960, doi:10.1175/BAMS-D-13-00093.1. http://journals.ametsoc.org/doi/abs/10.1175/BAMS-D-13-00093.1.

Bikos, D., and Coauthors, 2012: Synthetic Satellite Imagery for Real-Time High-Resolution Model Evaluation. *Weather Forecast.*, **27**, 784–795, doi:10.1175/WAF-D-11-00130.1. http://journals.ametsoc.org/doi/abs/10.1175/WAF-D-11-00130.1.

Brown, D. P., 2015: *National Hurricane Center Tropical Cyclone Report, Hurricane Gonzalo (AL082014) 12-19 October 2014.* Miami, Florida, 30 pp. http://www.nhc.noaa.gov/data/tcr/AL082014_Gonzalo.pdf.

Brown, P., C. Kummerow, and D. Randel, 2016: Hurricane GPROF: An optimized ocean microwave rainfall retrieval for Tropical. *J. Atmos. Ocean. Technol.*, (In Revision).

Chambon, P., S. Q. Zhang, A. Y. Hou, M. Zupanski, and S. Cheung, 2014: Assessing the impact of pre-GPM microwave precipitation observations in the Goddard WRF ensemble data assimilation system. *Q. J. R. Meteorol. Soc.*, **140**, 1219–1235, doi:10.1002/qj.2215. http://doi.wiley.com/10.1002/qj.2215.

Cotton, W. R., 1972: Numerical Simulation of Precipitation Development in Supercooled Cumuli - Part II. *Mon. Weather Rev.*, **100**, 764–784, doi:10.1175/1520-0493(1972)100<0764:NSOPDI>2.3.CO;2.

Emanuel, K. A., 1994: *Atmospheric Convection*. Oxford University Press, 580 pp.

Ferrier, B. S., 2005: An efficient mixed-phase cloud and precipitation scheme for use in operational NWP models. *Eos Trans AGU*, **86(18)**.

Grasso, L., D. T. Lindsey, K.-S. S. Lim, A. Clark, D. Bikos, and S. R. Dembek, 2014: Evaluation of and Suggested Improvements to the WSM6 Microphysics in WRF-ARW Using Synthetic and Observed GOES-13 Imagery. *Mon. Weather Rev.*, **142**, 3635–3650, doi:10.1175/MWR-D-14-00005.1.

Hence, D. A., and R. A. Houze, 2012: Vertical Structure of Tropical Cyclone Rainbands as Seen by the TRMM Precipitation Radar. *J. Atmos. Sci.*, **69**, 2644–2661, doi:10.1175/JAS-D-11-0323.1. http://journals.ametsoc.org/doi/abs/10.1175/JAS-D-11-0323.1 (Accessed April 15, 2014).

Hou, A. Y., S. Q. Zhang, and O. Reale, 2004: Variational Continuous Assimilation of TMI and SSM/I Rain Rates: Impact on GEOS-3 Hurricane Analyses and Forecasts. *Mon. Weather*

Rev., **132**, 2094–2109. http://dx.doi.org/10.1175/1520-0493(2004)132<2094:VCAOTA>2.0.CO;2.

Hou, A. Y., and Coauthors, 2014: The global precipitation measurement mission. *Bull. Am. Meteorol. Soc.*, **95**, 701–722, doi:10.1175/BAMS-D-13-00164.1.

Iguchi, T., T. Kozu, R. Meneghini, J. Awaka, and K. Okamoto, 2000: Rain-Profiling Algorithm for the TRMM Precipitation Radar. *J. Appl. Meteorol.*, **39**, 2038–2052, doi:10.1175/1520-0450(2001)040<2038:RPAFTT>2.0.CO;2.

Janjic, Z. I., 2003: A nonhydrostatic model based on a new approach. *Meteorol. Atmos. Phys.*, **82**, 271–285, doi:10.1007/s00703-001-0587-6.

Knaff, J. A., S. P. Longmore, and D. A. Molenar, 2014: An Objective Satellite-Based Tropical Cyclone Size Climatology. *J. Clim.*, **27**, 455–476, doi:10.1175/JCLI-D-13-00096.1. http://journals.ametsoc.org/doi/abs/10.1175/JCLI-D-13-00096.1 (Accessed March 28, 2014).

——, C. J. Slocum, K. D. Musgrave, C. R. Sampson, and B. Strahl, 2015: Using routinely available information to estimate tropical cyclone wind structure. *Mon. Weather Rev.*, in review and conditional accepted.

Kumar, P., C. M. Kishtawal, and P. K. Pal, 2014: Impact of satellite rainfall assimilation on Weather Research and Forecasting model predictions over the Indian region. *J. Geophys. Res. Atmos.*, **119**, 2017–2031, doi:10.1002/2013JD020005. http://www.scopus.com/inward/record.url?eid=2-s2.0-84898481948&partnerID=tZOtx3y1\nhttp://doi.wiley.com/10.1002/2013JD020005.

Kummerow, C., W. Barnes, T. Kozu, J. Shiue, and J. Simpson, 1998: The Tropical Rainfall Measuring Mission (TRMM) sensor package. *J. Atmos. Ocean. Technol.*, **15**, 809–817, doi:10.1175/1520-0426(1998)015<0809:TTRMMT>2.0.CO;2.

——, and Coauthors, 2001: The Evolution of the Goddard Profiling Algorithm (GPROF) for Rainfall Estimation from Passive Microwave Sensors. *J. Appl. Meteorol.*, **40**, 1801–1820, doi:10.1175/1520-0450(2001)040<1801:TEOTGP>2.0.CO;2.

Kummerow, C. D., D. L. Randel, M. Kulie, N. Y. Wang, R. Ferraro, S. Joseph Munchak, and V. Petkovic, 2015: The evolution of the goddard profiling algorithm to a fully parametric scheme. *J. Atmos. Ocean. Technol.*, **32**, 2265–2280, doi:10.1175/JTECH-D-15-0039.1.

Landsea, C. W., and J. L. Franklin, 2013: Atlantic Hurricane Database Uncertainty and Presentation of a New Database Format. *Mon. Weather Rev.*, **141**, 3576–3592, doi:10.1175/MWR-D-12-00254.1. http://journals.ametsoc.org/doi/abs/10.1175/MWR-D-12-00254.1 (Accessed February 4, 2014).

Lorenc, A. C., and F. Rawlins, 2005: Why does 4D-Var beat 3D-Var? *Q. J. R. Meteorol. Soc.*, **131**, 3247–3257, doi:10.1256/qj.05.85. http://doi.wiley.com/10.1256/qj.05.85.

Marchok, T. P., 2002: How the NCEP Tropical Cyclone Tracker Works. *25th Conference on Hurricanes and Tropical Meteorology* https://ams.confex.com/ams/25HURR/techprogram/paper_37628.htm.

Morrison, H., J. A. Curry, M. D. Shupe, and P. Zuidema, 2005: A New Double-Moment Microphysics Parameterization for Application in Cloud and Climate Models. Part II: Single-Column Modeling of Arctic Clouds. *J. Atmos. Sci.*, **62**, 1678–1693, doi:10.1175/JAS3447.1.

NOAA, 2010: NOAA's Next-Generation Strategic Plan. *Natl. Ocean. Atmos. Adm. Off. Progr. Plan. Integr.*, 40. http://www.ppi.noaa.gov/ngsp/.

Parrish, D. F., and J. C. Derber, 1992: The National Meteorological Center's Spectral Statistical-Interpolation Analysis System. *Mon. Weather Rev.*, **120**, 1747–1763, doi:10.1175/1520-0493(1992)120<1747:TNMCSS>2.0.CO;2.

Pu, Z.-X., W.-K. Tao, S. Branu, J. Simpson, Y. Jia, J. Halverson, W. Olson, and A. Hou, 2002: The Impact of TRMM Data on Numerical Forecast of Mesoscale Systems. 2448–2458.

Purser, R. J., W.-S. Wu, D. F. Parrish, and N. M. Roberts, 2003: Numerical Aspects of the Application of Recursive Filters to Variational Statistical Analysis. Part I: Spatially Homogeneous and Isotropic Gaussian Covariances. *Mon. Weather Rev.*, **131**, 1524–1535, doi:10.1175//1520-0493(2003)131<1524:NAOTAO>2.0.CO;2.

Rappaport, E. N., and Coauthors, 2009: Advances and Challenges at the National Hurricane Center. *Weather Forecast.*, **24**, 395–419, doi:10.1175/2008WAF2222128.1. http://journals.ametsoc.org/doi/abs/10.1175/2008WAF2222128.1.

Simpson, J., C. Kummerow, W.-K. Tao, and R. F. Adler, 1996: On the Tropical Rainfall Measuring Mission (TRMM). *Meteorol. Atmos. Phys.*, **60**, 19–36, doi:10.1007/BF01029783.

Stewart, S. R., 2013: *Tropical Cyclone Report, Hurricane Leslie (AL122012) 30 August - 11 September 2012*. Miami, Florida, 1-19 pp. http://www.nhc.noaa.gov/data/tcr/AL122012_Leslie.pdf.

Tallapragada, V., and Coauthors, 2014: Hurricane Weather Research and Forecasting (HWRF) Model: 2014 Scientific Documentation. *Dev. Testbed Cent.*, 1–96.

——, S. Gopalakrishnan, Q. Liu, and T. Marchok, 2015: Hurricane Weather Research and Forecasting (HWRF) model: 2011 scientific documentation. *Dev. Testbed Cent.*, 1–113. http://www.dtcenter.org/HurrWRF/users/docs/scientific_documents/HWRFScientificDocumentation_August2011.pdf.

Thompson, G., R. M. Rasmussen, and K. Manning, 2004: Explicit Forecasts of Winter Precipitation Using an Improved Bulk Microphysics Scheme. Part I: Description and Sensitivity Analysis. *Mon. Weather Rev.*, **132**, 519–542, doi:10.1175/1520-

0493(2004)132<0519:EFOWPU>2.0.CO;2.

Wang, X., 2010: Incorporating Ensemble Covariance in the Gridpoint Statistical Interpolation Variational Minimization: A Mathematical Framework. *Mon. Weather Rev.*, **138**, 2990–2995, doi:10.1175/2010MWR3245.1.

Wu, T.-C., H. Liu, S. J. Majumdar, C. S. Velden, and J. L. Anderson, 2014: Influence of Assimilating Satellite-Derived Atmospheric Motion Vector Observations on Numerical Analyses and Forecasts of Tropical Cyclone Track and Intensity. *Mon. Weather Rev.*, **142**, 49–71, doi:10.1175/MWR-D-13-00023.1. http://journals.ametsoc.org/doi/abs/10.1175/MWR-D-13-00023.1 (Accessed January 10, 2014).

Wu, W.-S., R. J. Purser, and D. F. Parrish, 2002: Three-Dimensional Variational Analysis with Spatially Inhomogeneous Covariances. *Mon. Weather Rev.*, **130**, 2905–2916, doi:10.1175/1520-0493(2002)130<2905:TDVAWS>2.0.CO;2.

Yablonsky, R. M., I. Ginis, B. Thomas, V. Tallapragada, D. Sheinin, and L. Bernardet, 2015: Description and Analysis of the Ocean Component of NOAA's Operational Hurricane Weather Research and Forecasting Model (HWRF). *J. Atmos. Ocean. Technol.*, **32**, 144–163, doi:10.1175/JTECH-D-14-00063.1.

Yu, H., T. Marchok, and W.-C. Woo, 2014: *Topic 8: Rainfall. WMO's Third International Workshop on Tropical Cyclones - Landfall Processes.* 1-8 pp.

Zhang, M., M. Zupanski, M.-J. Kim, and J. A. Knaff, 2013a: Assimilating AMSU-A Radiances in the TC Core Area with NOAA Operational HWRF (2011) and a Hybrid Data Assimilation System: Danielle (2010). *Mon. Weather Rev.*, **141**, 3889–3907, doi:10.1175/MWR-D-12-00340.1. http://journals.ametsoc.org/doi/abs/10.1175/MWR-D-12-00340.1.

Zhang, S. Q., M. Zupanski, A. Y. Hou, X. Lin, and S. H. Cheung, 2013b: Assimilation of Precipitation-Affected Radiances in a Cloud-Resolving WRF Ensemble Data Assimilation System. *Mon. Weather Rev.*, **141**, 754–772, doi:10.1175/MWR-D-12-00055.1. http://journals.ametsoc.org/doi/abs/10.1175/MWR-D-12-00055.1.

Zupanski, D., 1993: The effects of discontinuities in the Betts-Miller cumulus convection scheme on four-dimensional variational data assimilation. *Tellus A*, doi:10.3402/tellusa.v45i5.15053.

——, S. Q. Zhang, M. Zupanski, A. Y. Hou, and S. H. Cheung, 2011: A Prototype WRF-Based Ensemble Data Assimilation System for Dynamically Downscaling Satellite Precipitation Observations. *J. Hydrometeorol.*, **12**, 118–134, doi:10.1175/2010JHM1271.1. http://journals.ametsoc.org/doi/abs/10.1175/2010JHM1271.1 (Accessed April 21, 2014).

Tables.

Table 1. Constants used by the Clausius-Clapeyron equation.

C_1	C_2
$C_1^{ice} = -(S_{vapor} - S_{solid})/R_v$	$C_2^{ice} = C_1^{ice} + (L_{vapor} + L_{fusion}/R_v T_0)$
$C_1^{liquid} = -(S_{vapor} - S_{liquid})/R_v$	$C_2^{liquid} = C_1^{liquid} + (L_{vapor}/R_v T_0)$

S_{vapor} : specific heat of water vapor = 1.846×10^3 J kg^{-1} K^{-1}

S_{liquid} : specific heat of liquid water = 4.190×10^3 J kg^{-1} K^{-1}

S_{solid} : specific heat of ice water = 2.106×10^3 J kg^{-1} K^{-1}

R_v : gas constant of water vapor = 461.6 J kg^{-1} K^{-1}

L_{vapor} : latent heat of condensation = 2.5×10^6 J kg^{-1}

L_{fusion} : latent heat of fusion = 3.3358×10^5 J kg^{-1}

Table 2. Experimental design for assimilating Hurricane GPROF retrieved integrated SWC and LWC in the innermost domain of HWRF.

Experiment	Obs Assimilated in ghost d02		Obs Assimilated in ghost d03	
	Conventional	Satellite	Conventional	Satellite
CTL	x	x	x	None
AddWC	x	x	x	WC

Table 3. HWRF forecast experiments for Hurricanes Leslie (2012) and Gonzalo (2014).

Experiments	1st Cycle (yyyy/mm/dd hh)	2nd Cycle (yyyy/mm/dd hh)
	Hurricane Leslie (2012)	
L1 CTL & AddWC	2012/08/30 18 UTC	2012/08/31 00 UTC
	Hurricane Gonzalo (2014)	
G1 CTL & AddWC	2014/10/13 00 UTC	2014/10/13 06 UTC
G2 CTL & AddWC	2014/10/16 06 UTC	2014/10/16 12 UTC

Figure Captions

Figure 1: HWRF model forecast domains, as indicated by d01, d02, and d03, and HWRF data assimilation domains, as indicated by ghost d02 and ghost d03.

Figure 2: East-west cross-section of analysis increments (color) overlapped with background field (contour) along the latitude (21.8^{o}N) of the single observation location (open circle) from the no-hybrid 1-OBSSOLID experiment: (a) temperature (K) and (b) specific humidity (g kg^{-1}). (c) Analysis increments in surface pressure (hPa). (d) Cross-section of analysis increments in v-component of wind fields (m s^{-1}). (e)-(h) Same as (a)-(d) except for analysis increments from the no-hybrid 1-OBSLIQUID experiment. Background field contains Hurricane Leslie (2012) at 1800 UTC 2 September.

Figure 3: Same as Fig. 2 except for analysis increments from the hybrid (a-d) 1-OBSSOLID and (e-h) 1-OBSLIQUID experiments.

Figure 4: GOES-13 visible imagery at (a) 1215 UTC 5 September 2012 during Leslie and (b) 1307 UTC 16 October 2014 during Gonzalo.

Figure 5: Hurricane GPROF retrieved (a) integrated SWC (kg m^{-2}) and (b) integrated LWC (kg m^{-2}) assimilated in the L1 AddWC experiment during Leslie. (c)-(d) Same as (a)-(b) except for background guessed quantities. Similarly, (e)-(f) are estimated quantities from the L1 AddWC analysis. A bold magenta star marks the center of Leslie at the analysis time.

Figure 6: Same as Fig. 5, except for retrieved quantities that are assimilated in the G1 AddWC experiment during Gonzalo.

Figure 7: Same as Fig. 6, but for retrieved quantities that are assimilated in the G2 AddWC experiment during Gonzalo.

Figure 8: Vertical profiles of azimuthally-averaged (a) temperature (K), (b) specific humidity (g kg^{-3}), (c) tangential winds (m s^{-1}) and the radius of maximum winds (RMW, black contour), and (d) radial winds (m s^{-1}) from the L1 CTL analysis during Leslie. (e)-

(h) Same as (a)-(d) except for the L1 AddWC analysis. (i)-(l) are differences between the L1 CTL and the L1 AddWC analyses (L1 AddCW minus L1 CTL).

Figure 9: Same as Fig. 8, except for the G1 CTL and the G1 AddWC analyses during Gonzalo.

Figure 10: The 126-h HWRF forecast (a) track (km), size (km), (c) minimum mean sea level pressure (hPa), and (d) maximum 10-m winds (kt) initialized from the L1 CTL (blue) and the L1 AddWC (green) analyses during Leslie. Black solid lines represent the corresponding estimates from NHC best track data.

Figure 11: Same as Fig. 10, except for HWRF forecasts initialized from the G1 CTL and the G1 AddWC analyses during Gonzalo.

Figure 12: Same as Fig. 11, except for HWRF forecasts initialized from the G2 CTL and the G2 AddWC analyses during Gonzalo.

Figure 13: (a) PR measured (within black lines) and TMI estimated (outside black lines) rain rates (mm hr^{-1} in log scale) and column-integrated CWM (kg m^{-2} in log scale) from 18-h HWRF forecasts that are initialized from (b) the L1 CTL and (c) the L1 AddWC analyses during Leslie. (d) DPR measured (within black lines) and GMI estimated (outside black lines) rain rates (mm hr^{-1} in log scale). (e)-(f) Same as (b)-(c), except for

30-h HWRF forecasts that are initialized from the G1 CTL and the G1 AddWC analyses during Gonzalo. Similarly, (g)-(i) are results from 18-h HWRF forecasts that are initialized from the G2 CTL and the G2 AddWC analyses during Gonzalo. A bold magenta star marks hurricane center. The unit kg m^{-2} is equivalent to mm after dividing by density of liquid water, which is 1000 kg m^{-3}.

Figure 14: (a) GOES-13 10.7 μm infrared imagery and the corresponding synthetic satellite images (brightness temperature in Celsius degree) from 6-h HWRF forecasts that are initialized from (b) the L1 CTL and (c) the L1 AddWC analyses during Leslie. Regions of interest, d03 of HWRF, are shown in the dash box. (d)-(f) Same as (a)-(c) except for 6-h HWRF forecasts that are initialized from the G1 CTL and the G1 AddWC analyses during Gonzalo. Similarly, (g)-(i) are results from 6-h HWRF forecasts that are initialized from the G2 CTL and the G2 AddCW analyses during Gonzalo. A bold magenta star marks hurricane center in the GOES-13 image.

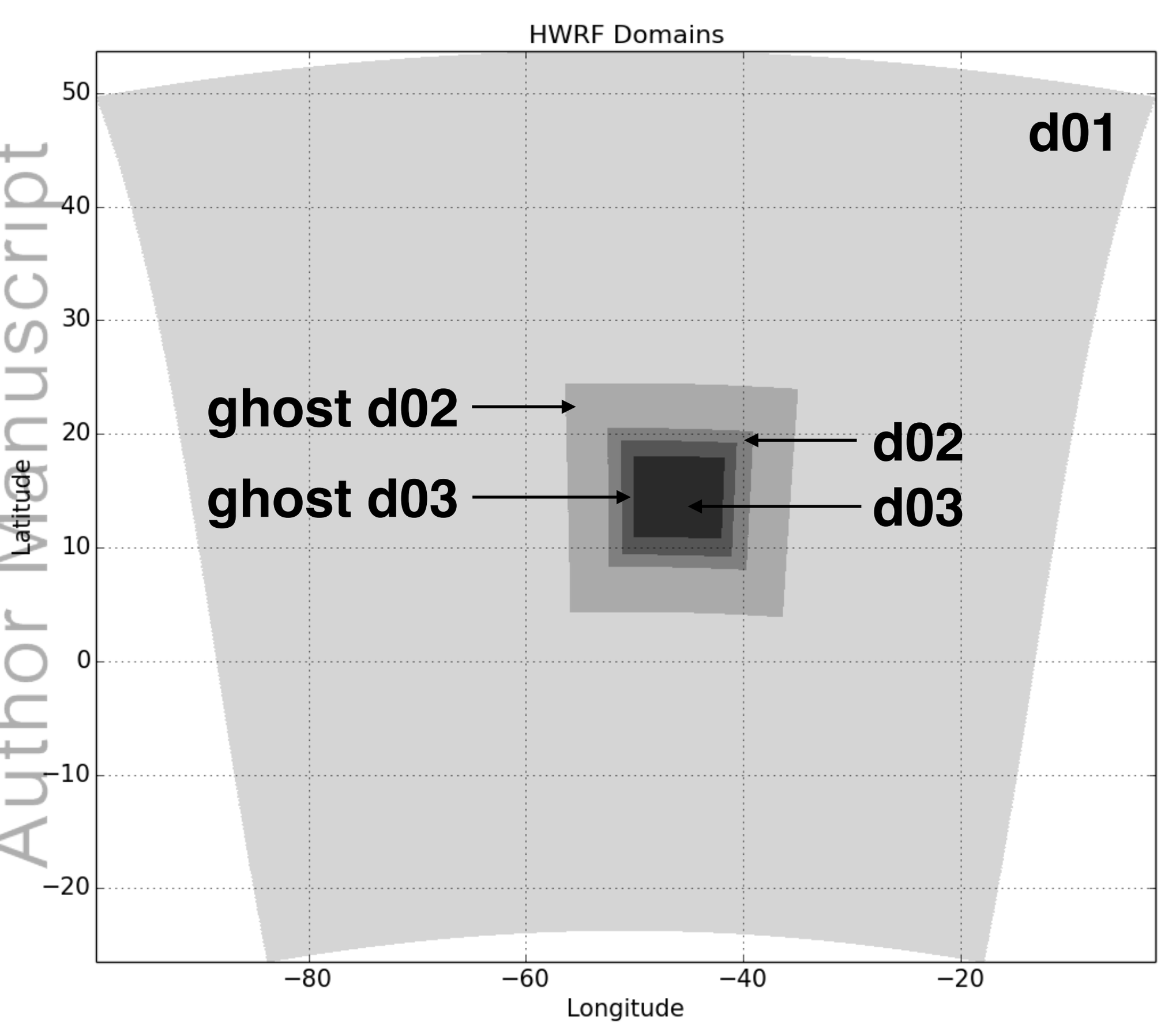

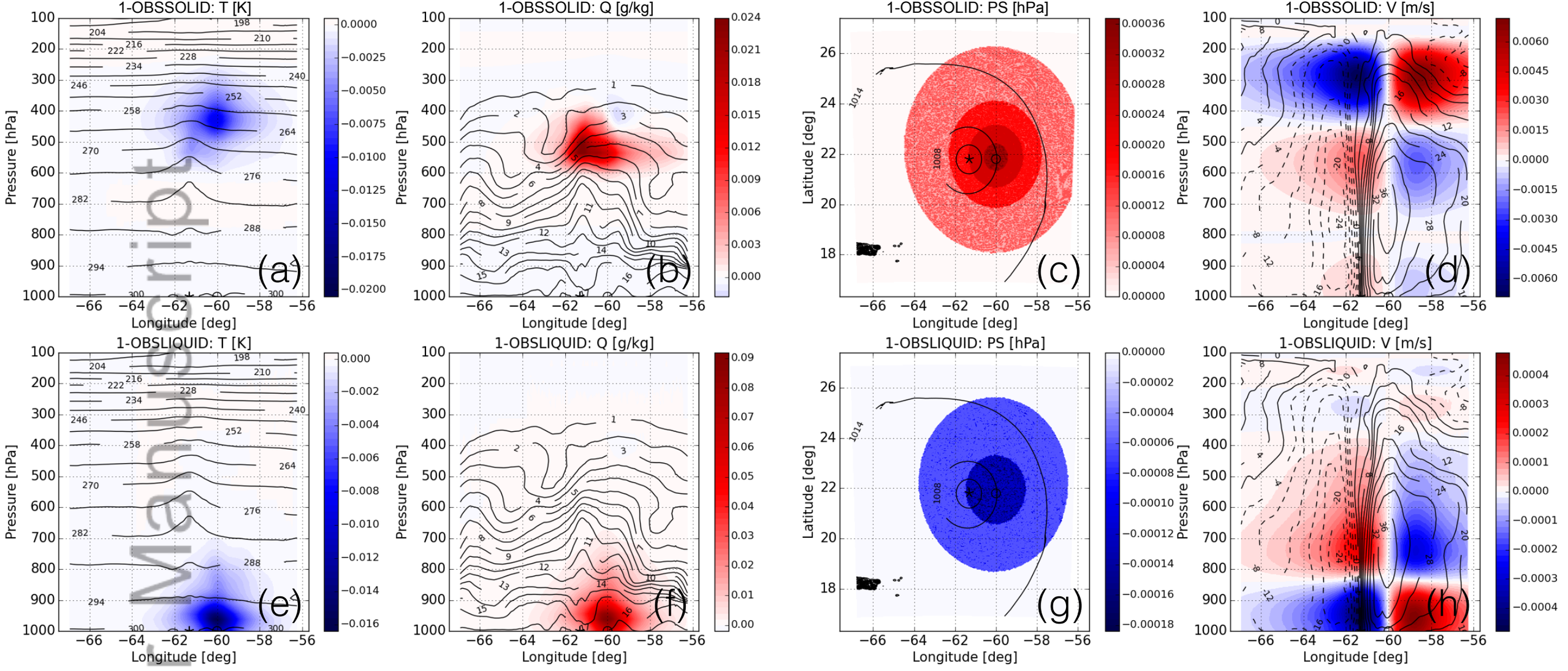
1-OBSSOLID: T [K]
1-OBSSOLID: Q [g/kg]
1-OBSSOLID: PS [hPa]
1-OBSSOLID: V [m/s]
1-OBSLIQUID: T [K]
1-OBSLIQUID: Q [g/kg]
1-OBSLIQUID: PS [hPa]
1-OBSLIQUID: V [m/s]
Pressure [hPa]
Latitude [deg]
Longitude [deg]
(a)
(b)
(c)
(d)
(e)
(f)
(g)
(h)
Manuscript

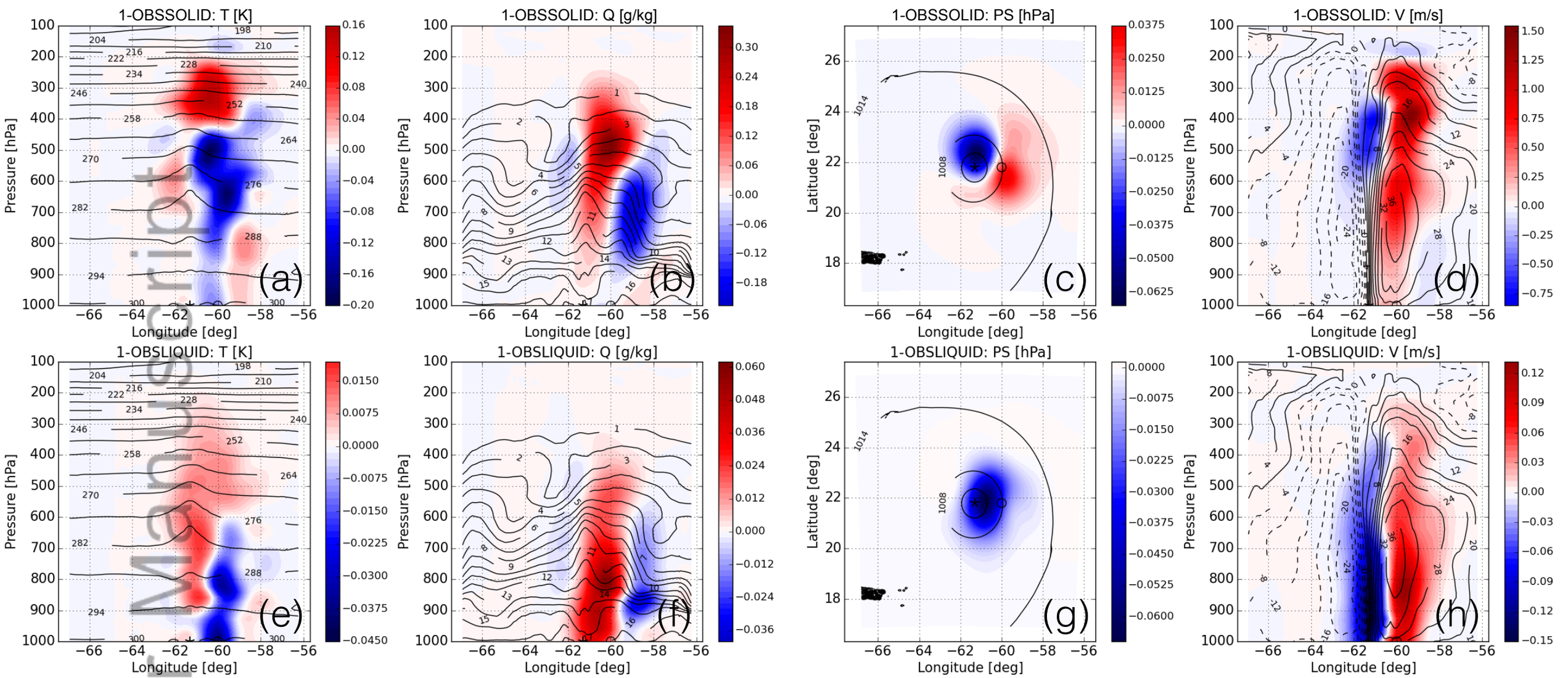
1-OBSSOLID: T [K]
1-OBSSOLID: Q [g/kg]
1-OBSSOLID: PS [hPa]
1-OBSSOLID: V [m/s]
1-OBSLIQUID: T [K]
1-OBSLIQUID: Q [g/kg]
1-OBSLIQUID: PS [hPa]
1-OBSLIQUID: V [m/s]
Pressure [hPa]
Latitude [deg]
Longitude [deg]
(a)
(b)
(c)
(d)
(e)
(f)
(g)
(h)

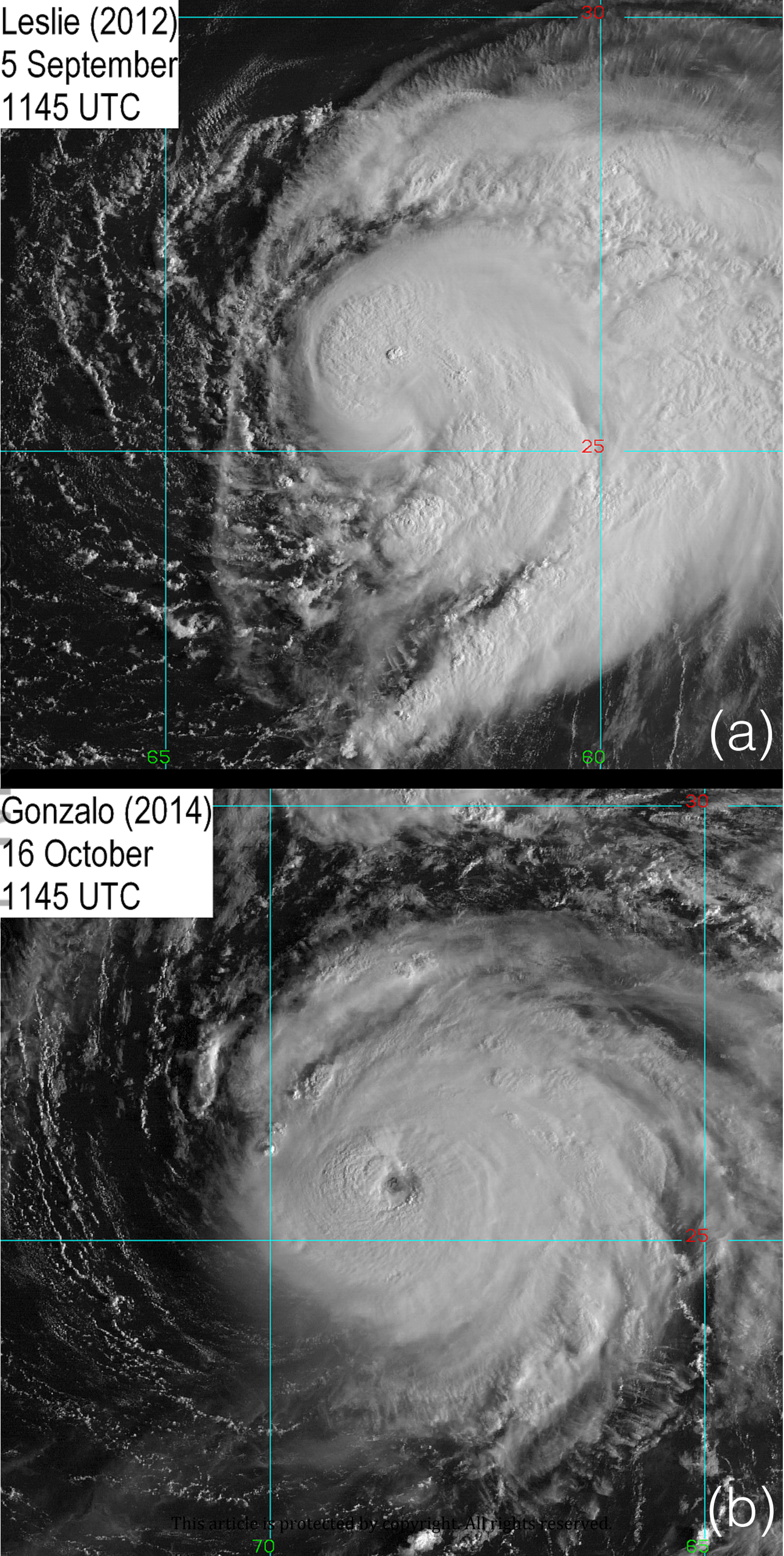

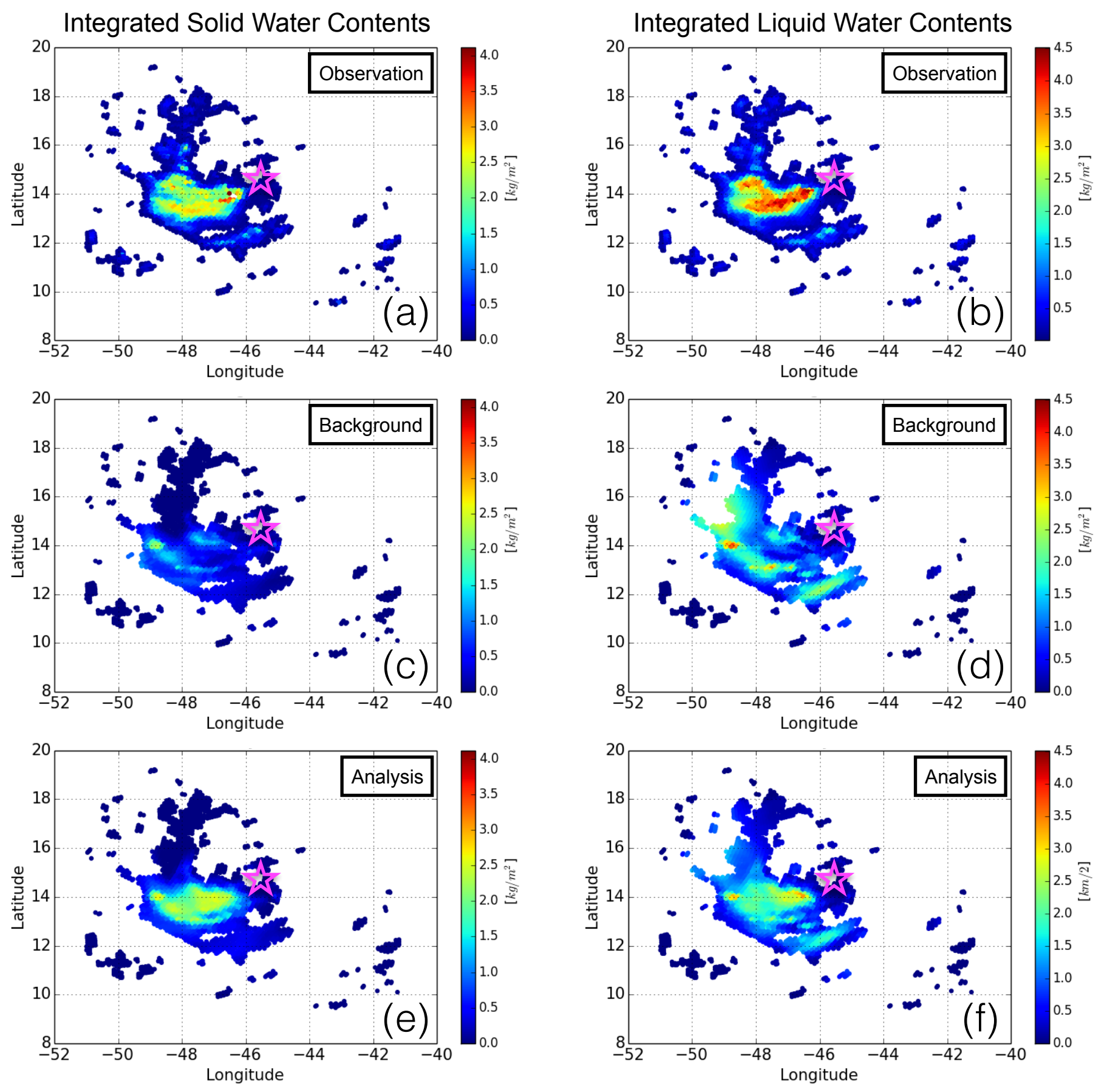
Integrated Solid Water Contents
Integrated Liquid Water Contents
Observation
Background
Analysis
(a)
(b)
(c)
(d)
(e)
(f)
Latitude
Longitude
$[kg/m^2]$
$[km/2]$

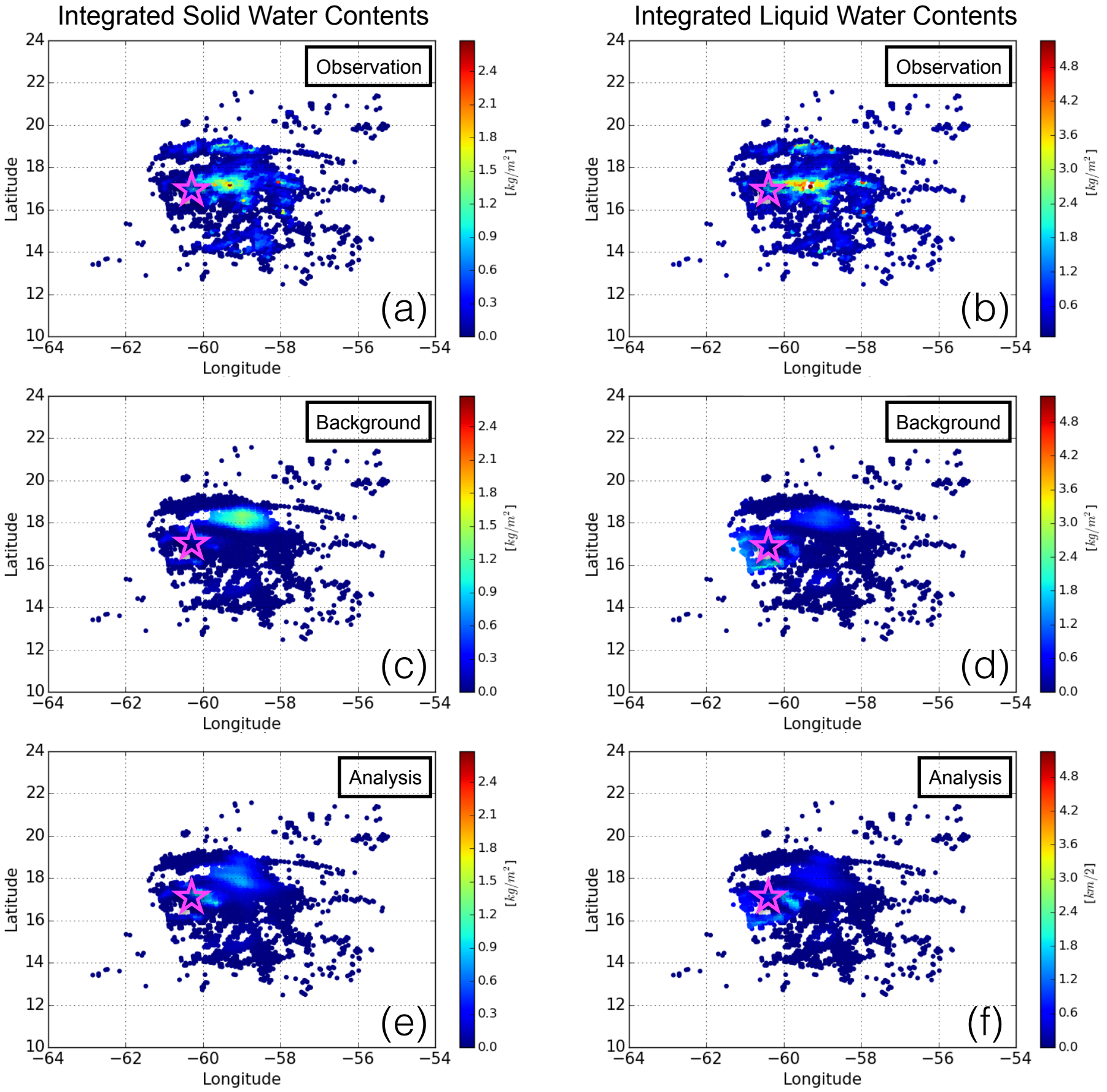
Integrated Solid Water Contents
Integrated Liquid Water Contents
Observation
Background
Analysis
(a)
(b)
(c)
(d)
(e)
(f)
Latitude
Longitude
24
22
20
18
16
14
12
10
−64
−62
−60
−58
−56
−54
$[kg/m^2]$
$[km/2]$
0.0
0.3
0.6
0.9
1.2
1.5
1.8
2.1
2.4
3.0
3.6
4.2
4.8

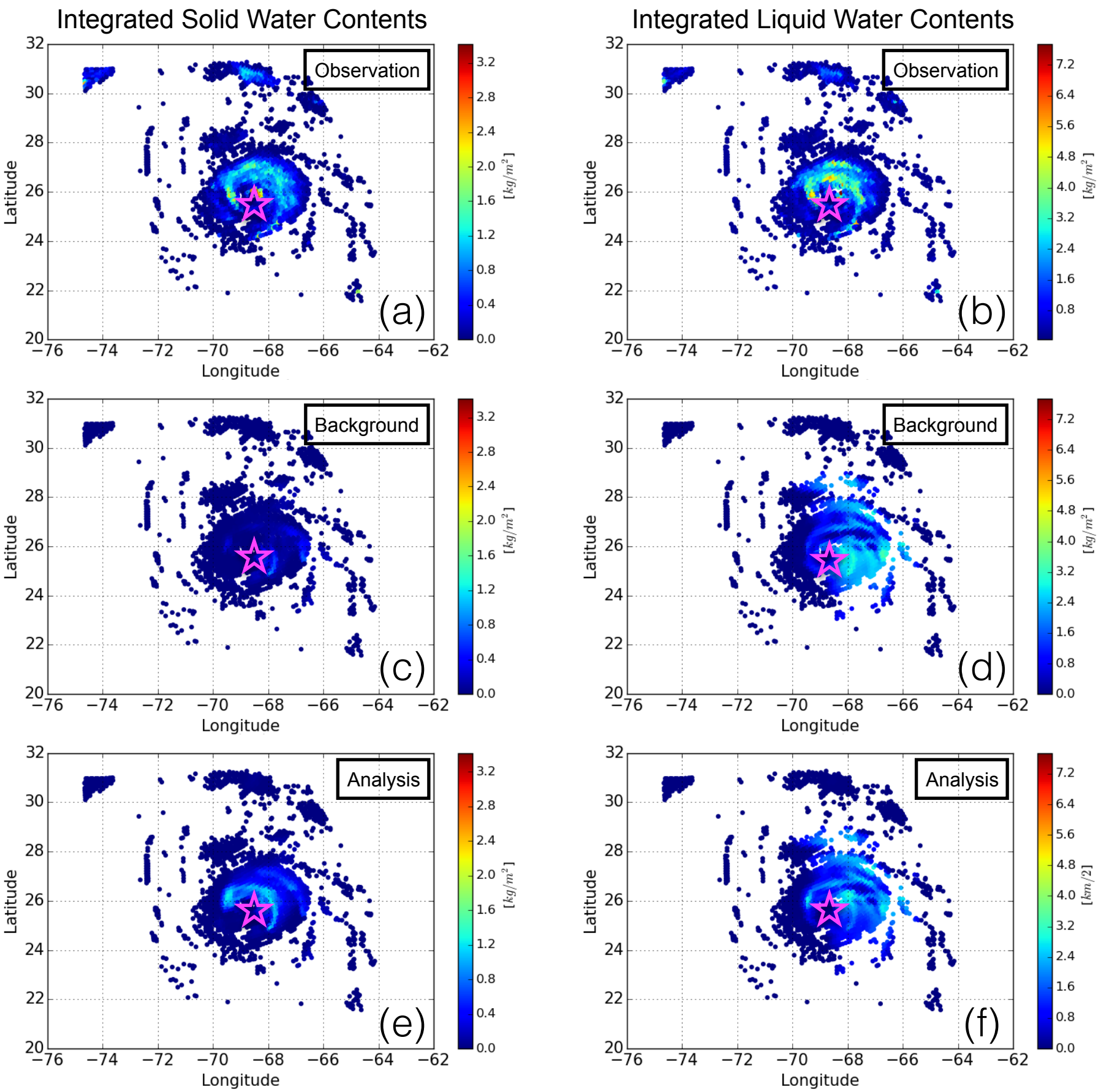
Integrated Solid Water Contents
Integrated Liquid Water Contents
Observation
Background
Analysis
(a)
(b)
(c)
(d)
(e)
(f)
Latitude
Longitude
[kg/m²]
[km/2]

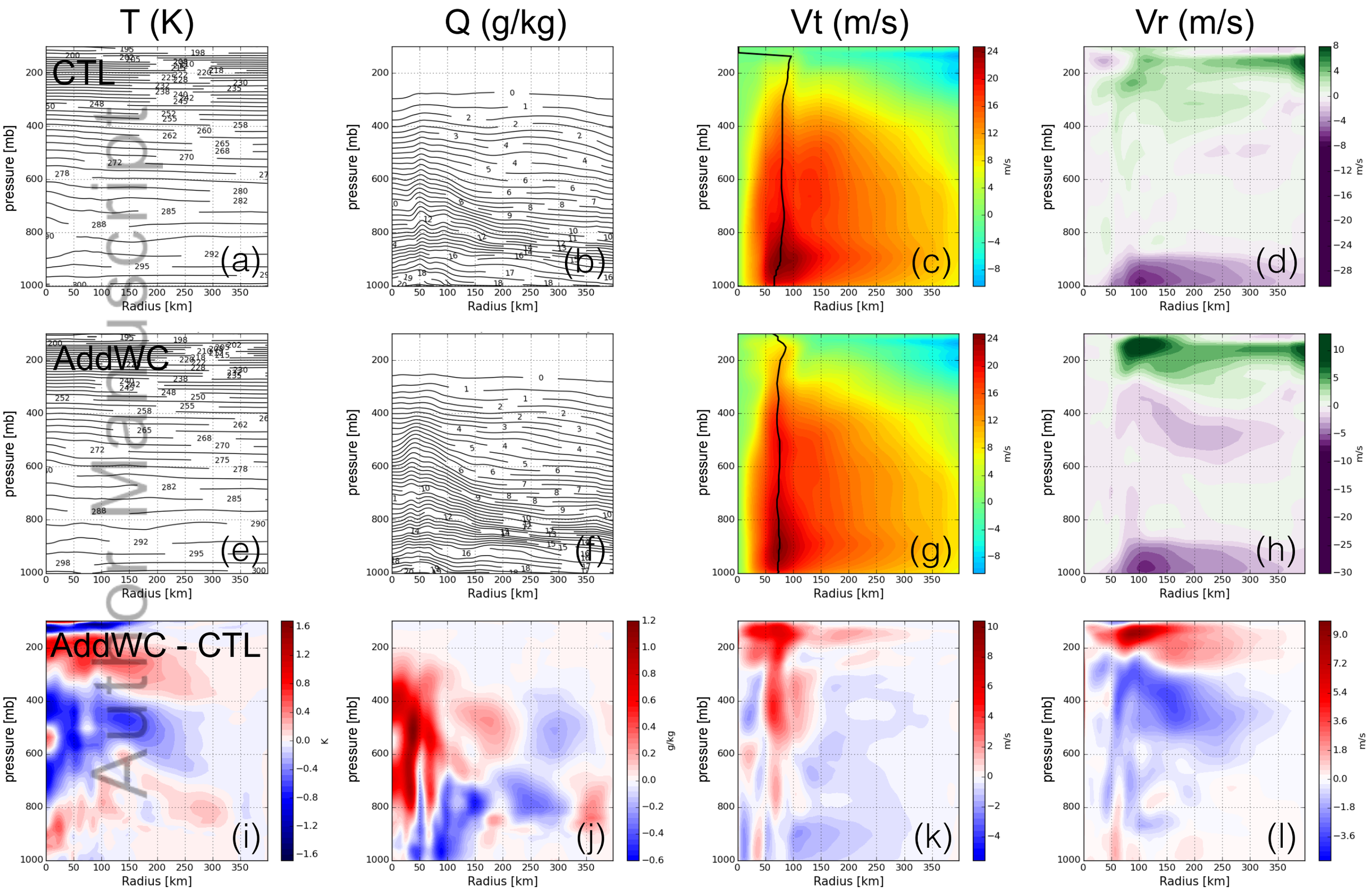

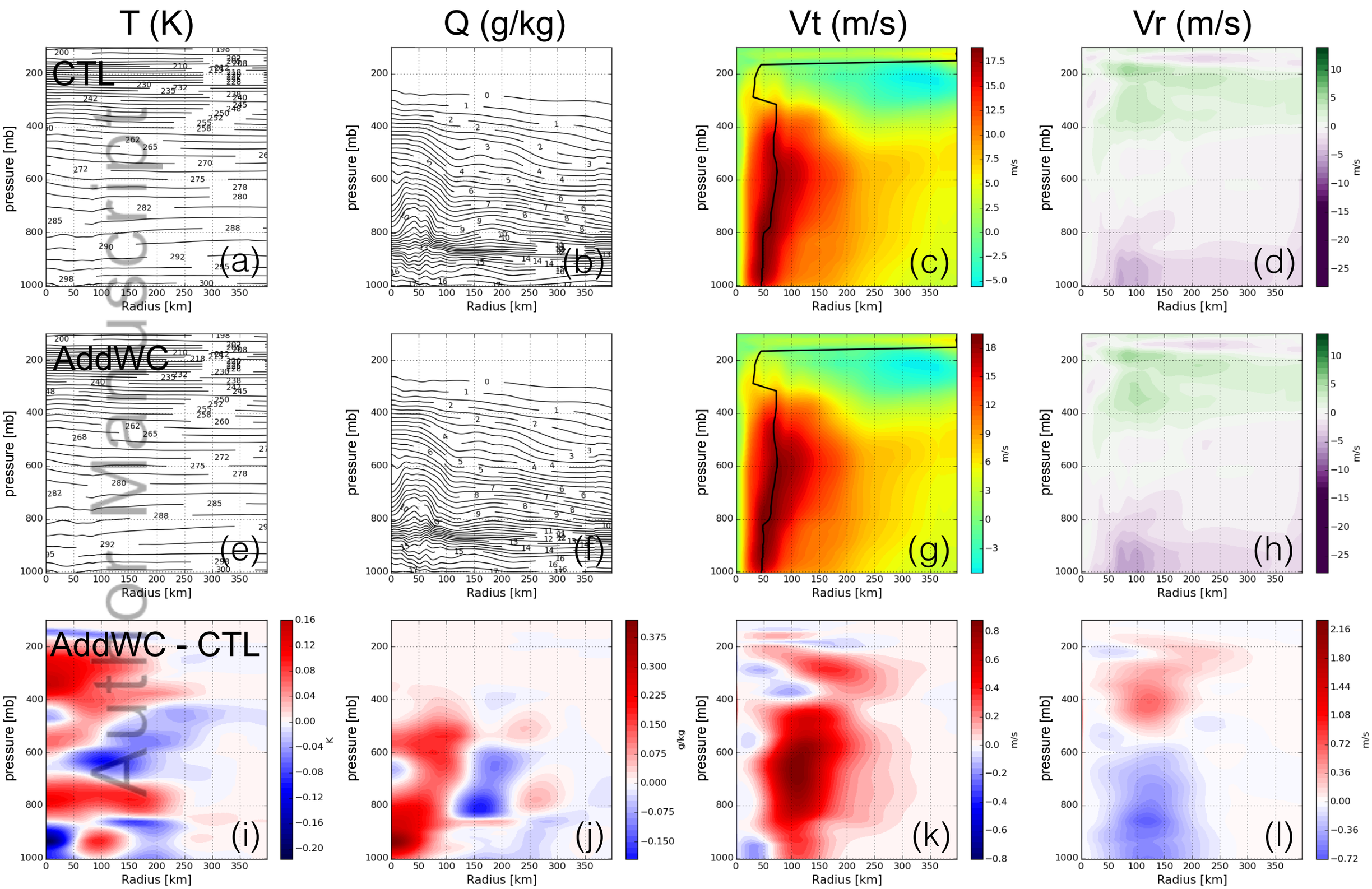

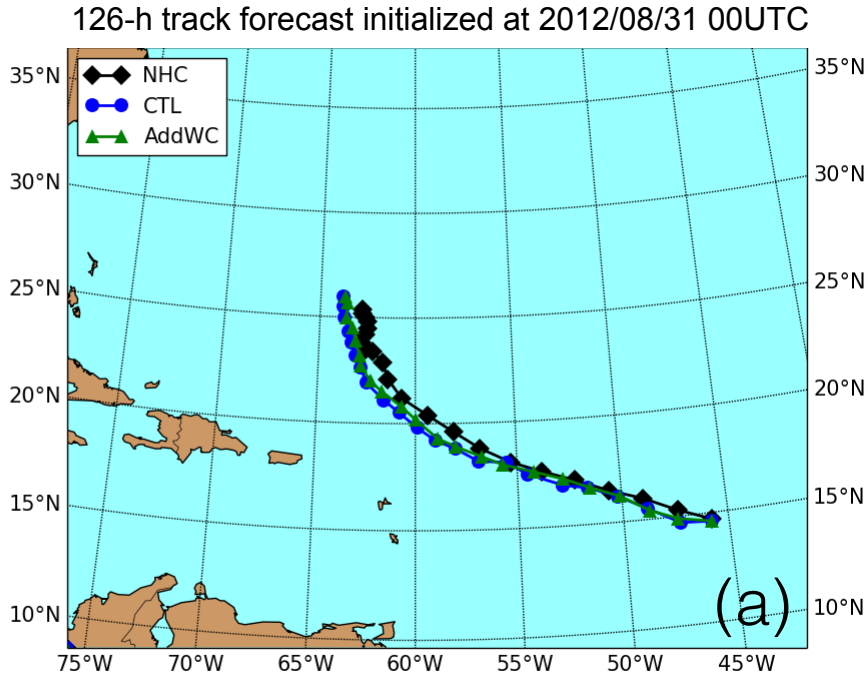

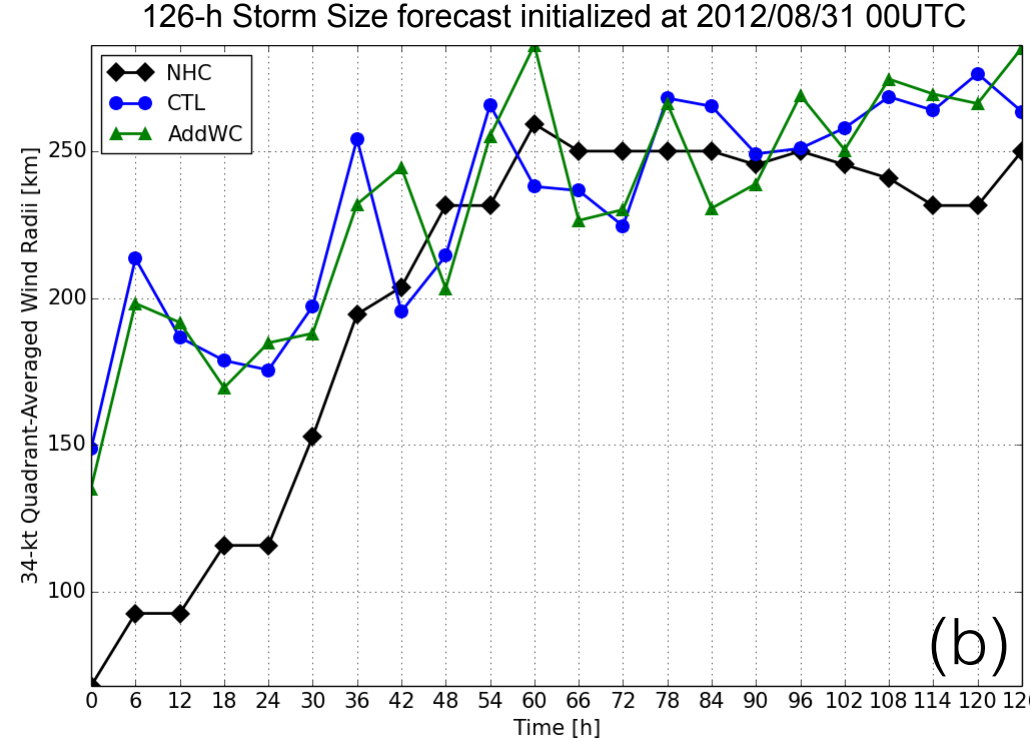

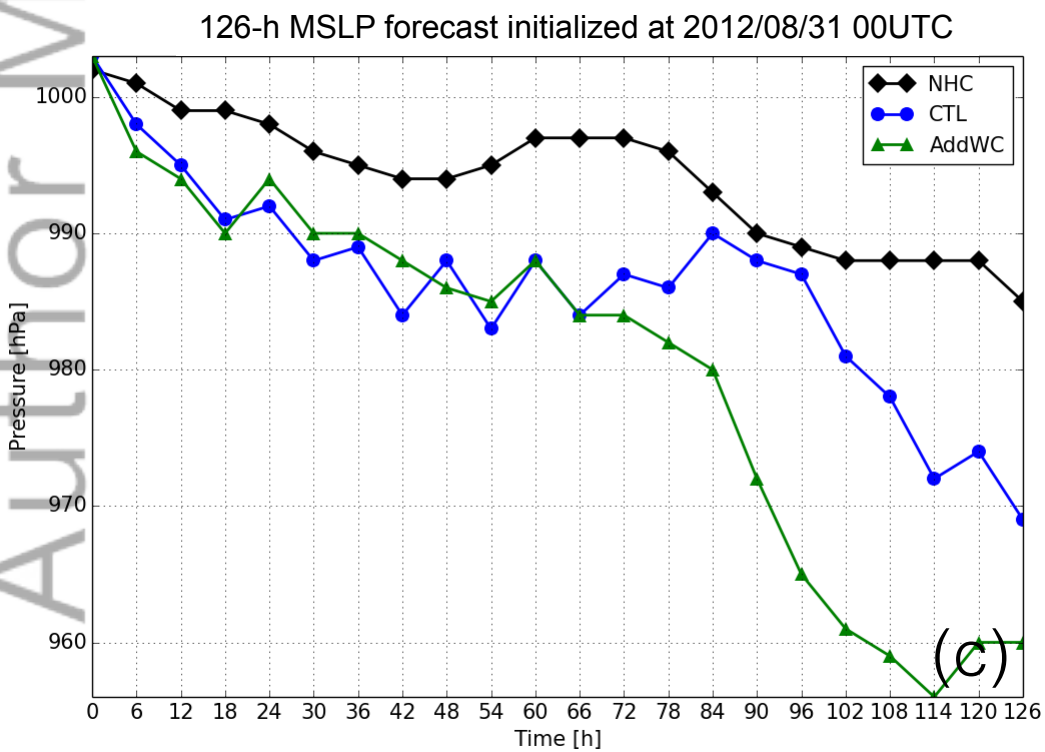

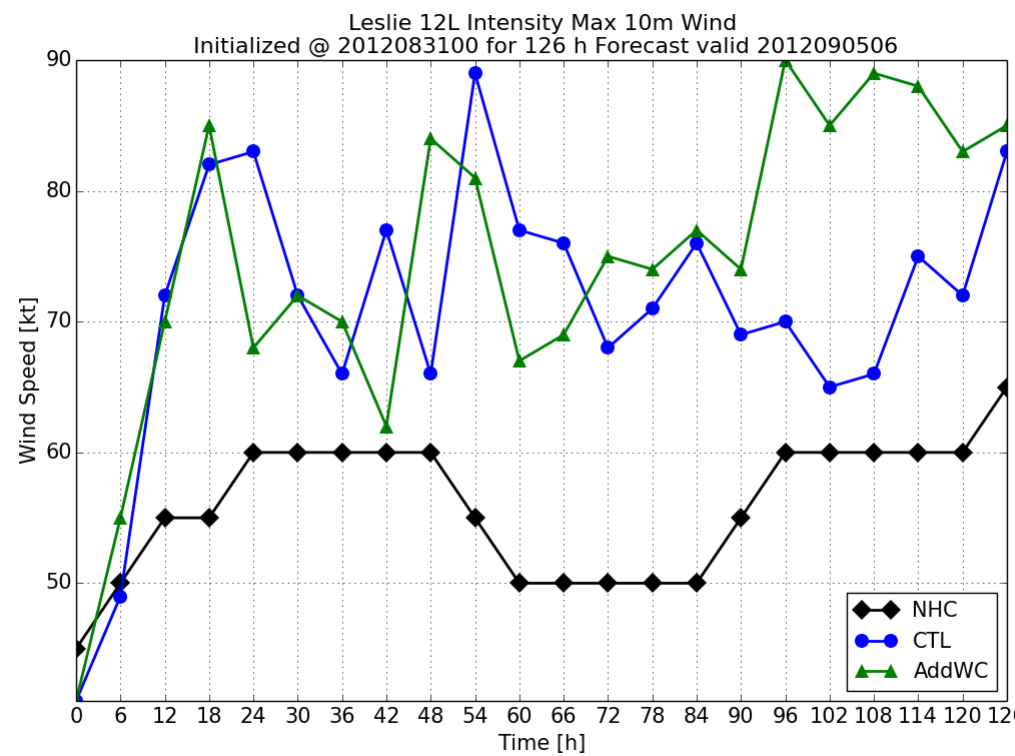

126-h track forecast initialized at 2014/10/13 06UTC

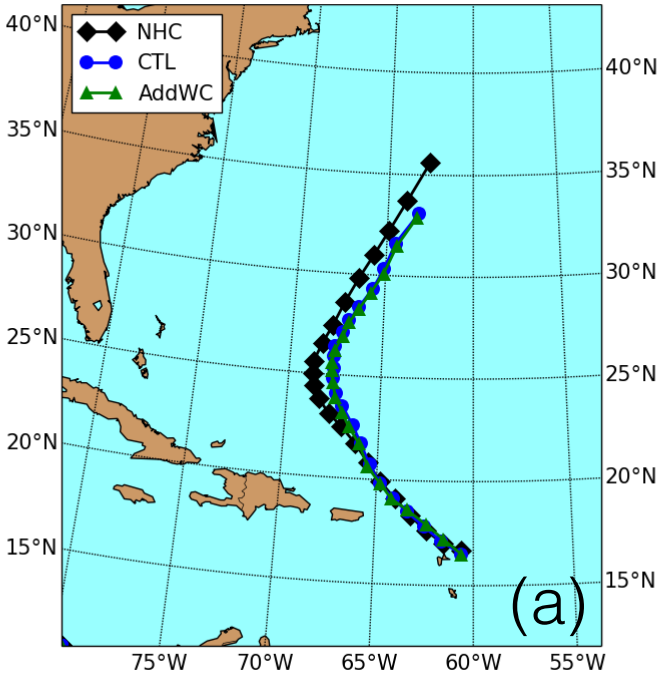

126-h Storm Size forecast initialized at 2014/10/13 06UTC

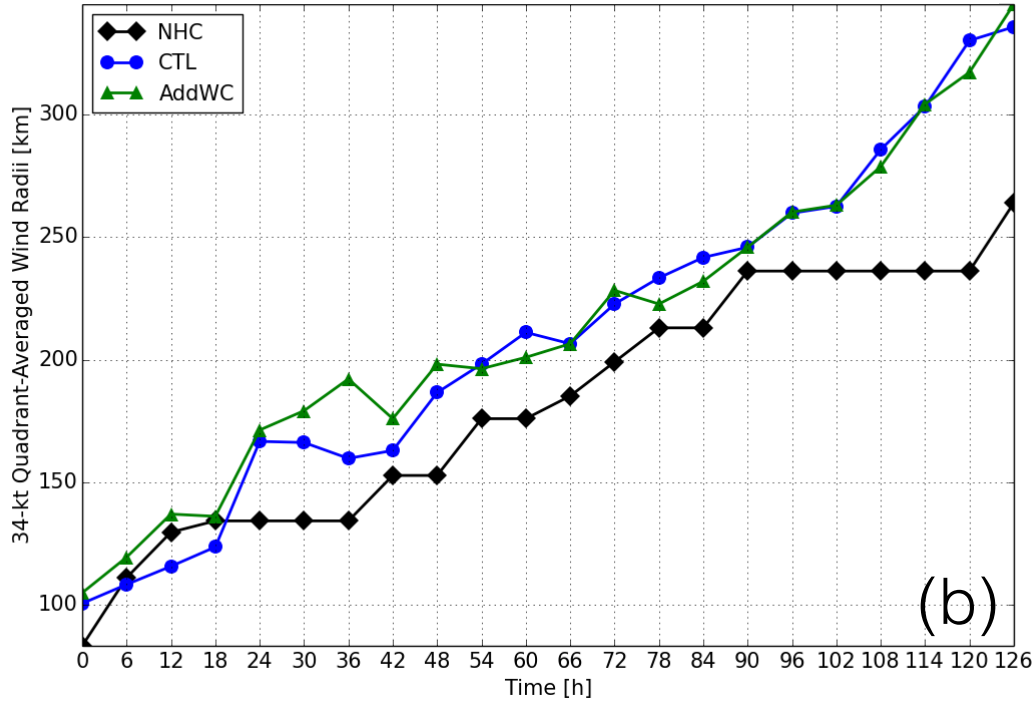

126-h MSLP forecast initialized at 2014/10/13 06UTC

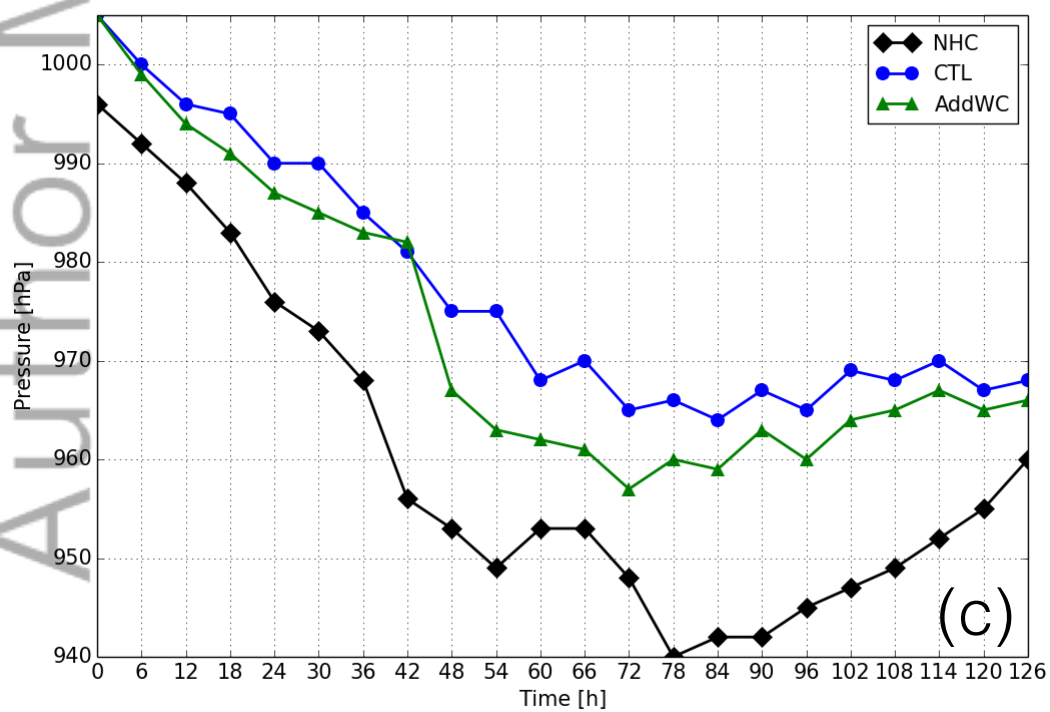

Gonzalo 08L Intensity Max 10m Wind
Initialized @ 2014101306 for 126 h Forecast valid 2014101812

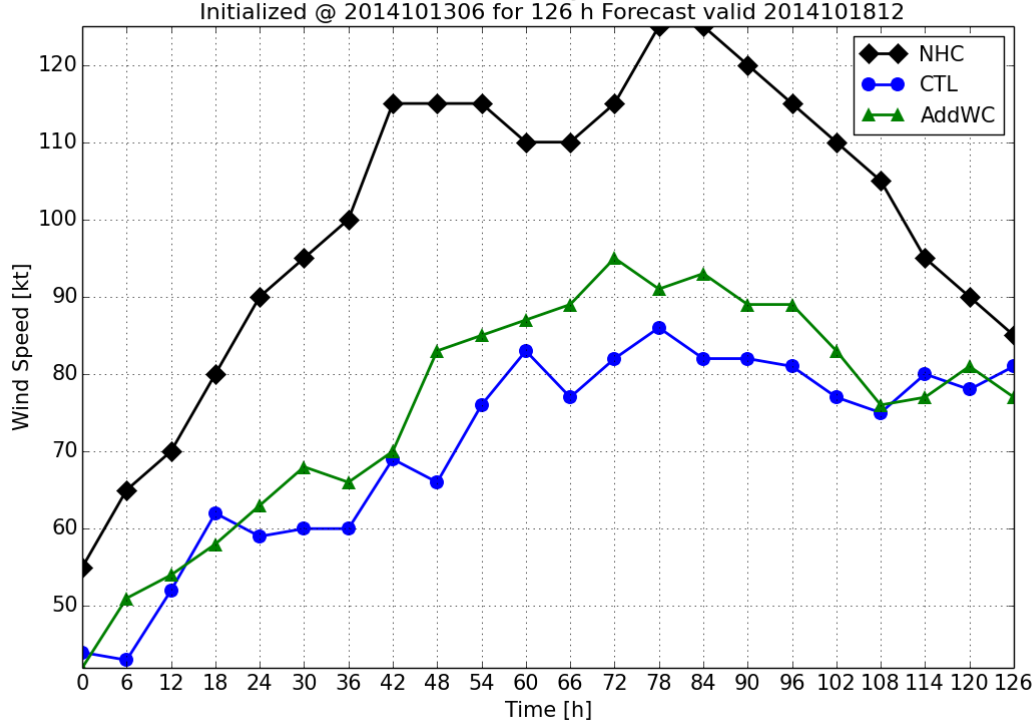

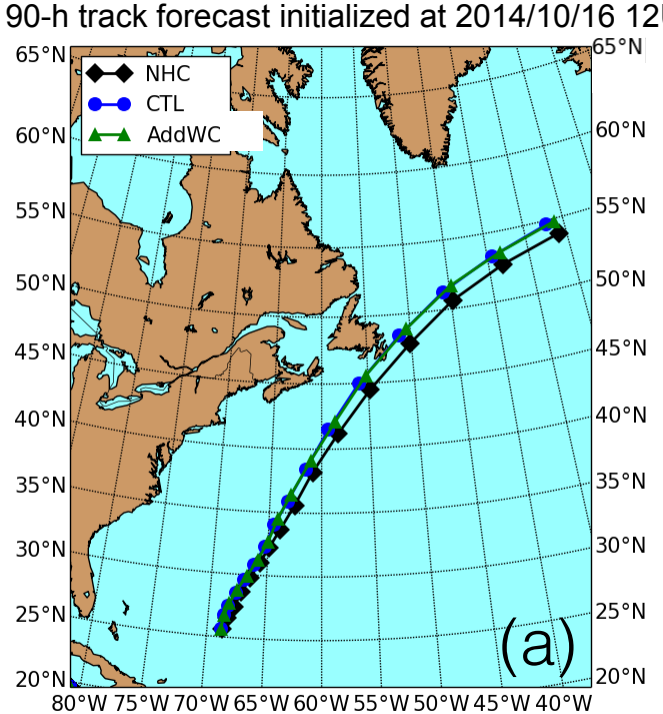
90-h track forecast initialized at 2014/10/16 12UTC
NHC
CTL
AddWC
(a)
65°N
60°N
55°N
50°N
45°N
40°N
35°N
30°N
25°N
20°N
80°W 75°W 70°W 65°W 60°W 55°W 50°W 45°W 40°W

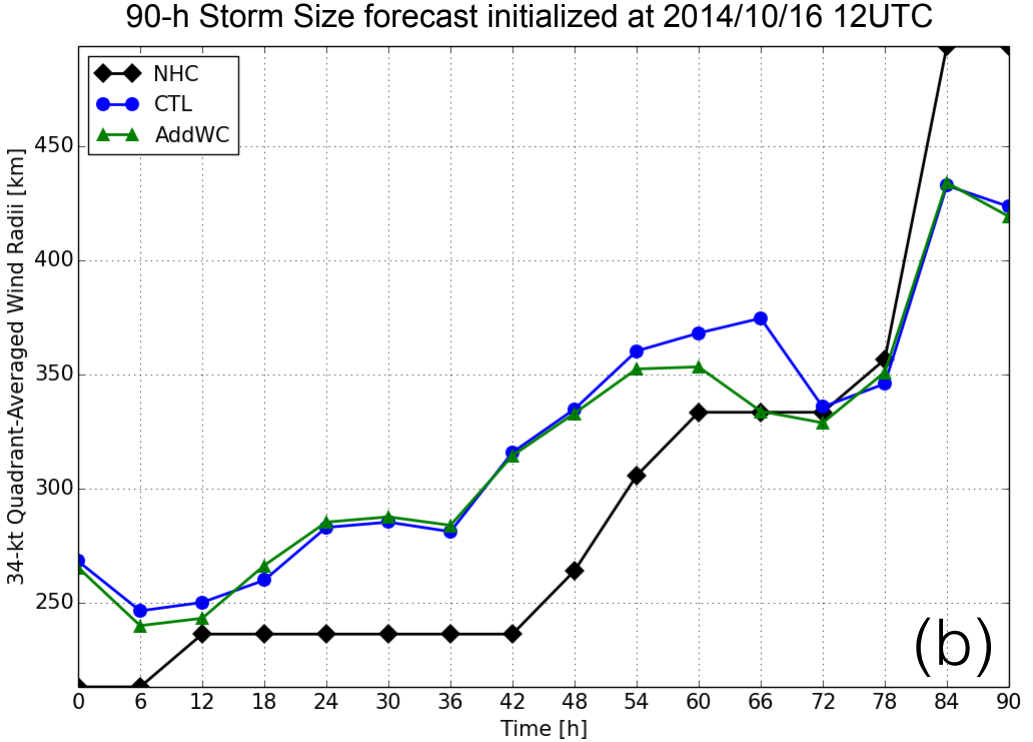
90-h Storm Size forecast initialized at 2014/10/16 12UTC
NHC
CTL
AddWC
34-kt Quadrant-Averaged Wind Radii [km]
250
300
350
400
450
(b)
0 6 12 18 24 30 36 42 48 54 60 66 72 78 84 90
Time [h]

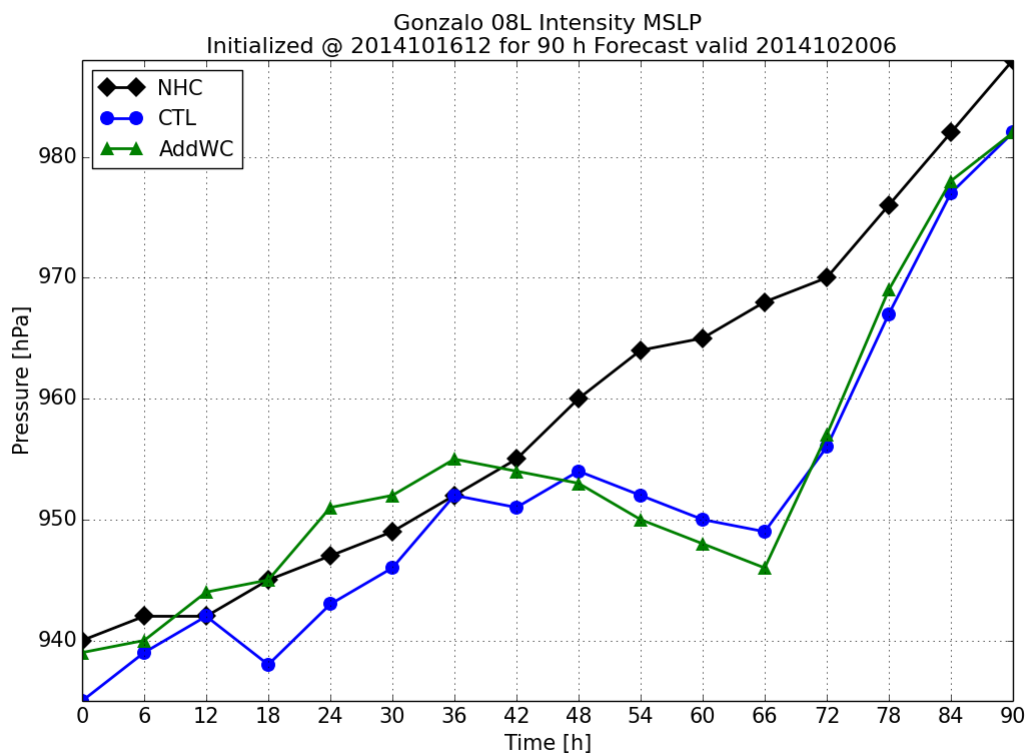
Gonzalo 08L Intensity MSLP
Initialized @ 2014101612 for 90 h Forecast valid 2014102006
NHC
CTL
AddWC
Pressure [hPa]
940
950
960
970
980
0 6 12 18 24 30 36 42 48 54 60 66 72 78 84 90
Time [h]

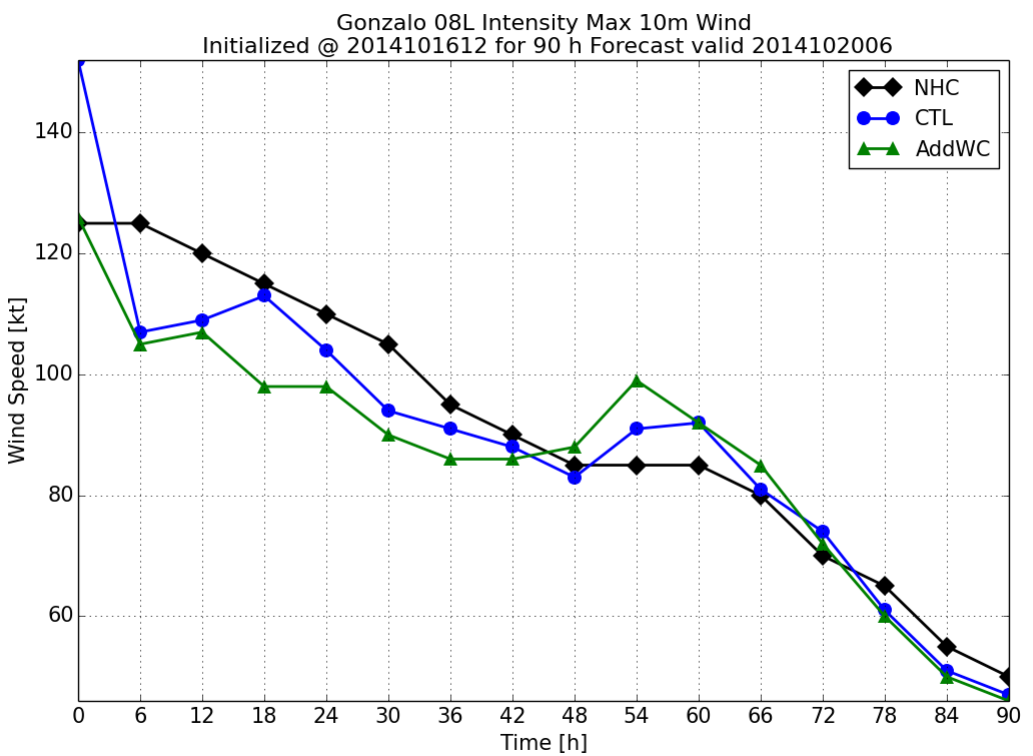
Gonzalo 08L Intensity Max 10m Wind
Initialized @ 2014101612 for 90 h Forecast valid 2014102006
NHC
CTL
AddWC
Wind Speed [kt]
60
80
100
120
140
0 6 12 18 24 30 36 42 48 54 60 66 72 78 84 90
Time [h]